

Occupation Resolved Conductance of a Few Electron Quantum Dot

**A Test for Kondo Correlations in an Intermediate
Coupling Regime**

by

Johann Peter Drayne

B.Sc., The University of British Columbia, 2022

A THESIS SUBMITTED IN PARTIAL FULFILLMENT OF
THE REQUIREMENTS FOR THE DEGREE OF

MASTER OF SCIENCE

in

THE FACULTY OF GRADUATE AND POSTDOCTORAL STUDIES
(Physics)

THE UNIVERSITY OF BRITISH COLUMBIA

(Vancouver)

April 2024

© Johann Peter Drayne 2024

The following individuals certify that they have read, and recommend to the Faculty of Graduate and Postdoctoral Studies for acceptance, the thesis entitled:

Occupation Resolved Conductance of a Few Electron Quantum Dot: A Test for Kondo Correlations in an Intermediate Coupling Regime

submitted by **Johann Peter Drayne** in partial fulfillment of the requirements for the degree of **Master of Science in Physics**.

Examining Committee:

Joshua Folk, Professor, Physics and Astronomy, UBC
Supervisor

Alannah Hallas, Assistant Professor, Physics and Astronomy, UBC
Supervisory Committee Member

Abstract

The Kondo effect, first discovered in impure bulk metals during the 1930s and explained in the 1960s, has gained significant interest within the field of quantum devices. These devices offer a high degree of tunability and control, enabling rigorous testing of theoretical predictions. Previous studies on the Kondo effect have measured conductance through a quantum dot and observed a zero-bias peak between Coulomb peaks. This effect requires strong coupling between the quantum dot and leads.

This work studies a relatively weak coupling, where the characteristic zero-bias peak between Coulomb peaks is not observed. However, as charge degeneracy of the quantum dot is approached, the Kondo temperature increases. This results in a small conductance enhancement at the shoulder of the Coulomb peak. We show that a simultaneous measurement of the quantum dot's occupation can unveil the small enhancement of conductance due to the Kondo effect.

To compare with Numerical Renormalisation Group (NRG) theory, conductance and occupation are measured across a range of temperatures to determine fitting parameters. Good agreement is found at a range of coupling strengths and charge sensor current setpoints. However, a discrepancy is found when the tunnel barriers to the quantum dot are asymmetrically tuned.

Strong asymmetric coupling approaches a regime where the quantum dot is coupled to a single lead. A recent measurement of the entropy of a quantum dot coupled to a single lead where Kondo correlations were expected also observed a discrepancy between data and NRG. Interestingly, this work shows that conductance data displays greater Kondo enhancement than NRG, whereas previously measured entropy showed less Kondo

Abstract

enhancement than NRG. A direct comparison of conductance and entropy measured in the same device under similar settings holds promise for illuminating this discrepancy.

Lay Summary

The Kondo effect, a phenomenon originally observed in impure metals decades ago, has been studied more recently in quantum devices. These devices offer precise control to test theoretical predictions. In these devices, a single electron on an isolated island is connected to a bath of electrons on each side.

Previous studies have measured the conductance through the island as a single electron is added and observed a large increase in conductance as the system's temperature was lowered. These experiments used a small barrier between the island and surrounding electrons.

In our experiment, we used a large barrier, resulting in an increase in conductance that was too small to measure with previous methods. To measure this small increase in conductance, we also measure the island's occupation as a single electron is added. When the barriers to the island are symmetric, we find agreement with theory, and surprising disagreement when asymmetric.

Preface

This thesis encompasses the research I conducted during my Master's studies in the Quantum Devices group, led by Joshua Folk, at the University of British Columbia.

Numerous discussions with my supervisor Joshua Folk, and research associate Silvia Lüscher have greatly influenced the experimental concept, device design, analysis and interpretation.

The GaAs/AlGaAs heterostructures were provided by Michael Manfra's group at the University of Purdue. Christian Olsen fabricated the mesas and ohmic contacts at the University of Copenhagen.

Numerical Renormalisation Group (NRG) simulations that we compare our measurements to in Chapter 4, were performed by Yaakov Kleeorin, under the supervision of Yigal Meir.

I joined the Quantum Devices group as an undergraduate (September 2021) and spent the first eight months shadowing Timothy Child throughout the design, fabrication, measurement, and analysis processes.

The following year (first year of my Master's studies, September 2022), I spent working closely with Timothy on device design, fabrication, and measurement. Timothy and I fabricated all devices used in this thesis during this period. All data taken in Chapter 2 and Chapter 3 was taken by Timothy and I. In particular, at the end of this period, Timothy and I took preliminary measurements in the regime explored in Chapter 4. These measurements demonstrated a working proof of how to measure in this regime.

In my final year (starting May 2023), Timothy worked on his PhD, and I became the lead researcher responsible for data collection and analysis. All data taken in Chapter 4 was taken during this period.

All figures in this work are original.

Table of Contents

Abstract	iii
Lay Summary	v
Preface	vi
Table of Contents	vii
List of Tables	x
List of Figures	xi
Acknowledgements	xiii
Dedication	xvi
1 Introduction	1
1.1 Context	1
1.2 Outline	4
2 Device Background	5
2.1 Introduction	5
2.2 Two Dimensional Electron Gas (2DEG)	5
2.3 Quantum Point Contact (QPC)	7
2.4 Quantum Dot	10
2.4.1 Conductance Through a Quantum Dot	11
2.4.2 Charge Sensing a Quantum Dot	13
2.5 Determining Electron Temperature	15

Table of Contents

2.6	Measurement Procedures	17
2.6.1	Cooldown Bias	17
2.6.2	Gate Divider	18
2.6.3	Virtual Gate	18
3	Conductance in the Kondo Regime	21
3.1	Introduction	21
3.2	Kondo Effect in Bulk Materials	21
3.3	Kondo Effect in Quantum Dots	23
4	Occupation Resolved Conductance of the Kondo Effect	28
4.1	Introduction	28
4.2	Occupation Resolved Conductance Method	30
4.2.1	Numerical Renormalisation Group (NRG)	32
4.2.2	Conductance Global Fit to NRG	33
4.2.3	Charge Transition Fit to NRG	33
4.2.4	Determining Occupation	34
4.2.5	Conductance versus Occupation	36
4.3	Kondo Effect with Varying Coupling Strength	36
4.4	Kondo Effect with Varying Charge Sensor Current	38
4.4.1	Varying Charge Transition	38
4.4.2	Conductance versus Occupation	39
4.5	Kondo Effect with Varying Coupling Symmetry	41
4.5.1	Symmetric to Asymmetric Coupling	41
4.5.2	Conductance versus Occupation	44
5	Conclusion	47

Appendices

A	Quantum Device Fabrication	60
A.1	Summary	60
A.2	Recipes	61
A.2.1	Gallium Removal	61

Table of Contents

A.2.2	Mesa Etch	62
A.2.3	Ohmic Contact	62
A.2.4	Gating	64
A.2.5	Wire Bonding	66
B	Software	68
B.1	Open-Source Thesis	68
B.2	Data Acquisition and Analysis	68
B.3	Device Simulation	68

List of Tables

4.1 $\Gamma/k_B T$ From Conductance and Charge Transition Global Fits 43

List of Figures

1.1	Fridge to Quantum Dot Scale Illustration	2
2.1	GaAs/AlGaAs Heterostructure	6
2.2	Quantum Point Contact	8
2.3	Quantum Dot Energy Levels	10
2.4	Conductance Through a Quantum Dot	12
2.5	Charge Sensing a Quantum Dot	14
2.6	Determining Electron Temperature	15
2.7	Effects of a Virtual Gate	19
3.1	Kondo Effect in Bulk Materials	22
3.2	Kondo Effect Illustration : Bulk Material	23
3.3	Kondo Effect Illustration : Quantum Dot	24
3.4	Kondo Effect in a Strongly Coupled Quantum Dot	26
4.1	Fittin Conductance and Charge Transition to NRG	34
4.2	Conductance versus Occupation : Varying Temperature	35
4.3	Conductance versus Occupation : Varying Coupling Strength	37
4.4	Varying Charge Sensor Current Setpoint	39
4.5	Conductance versus Occupation : Varying Charge Sensor Current	40
4.6	Symmetric to Asymmetric Coupling	42
4.7	Conductance versus Occupation : Varying Coupling Symmetry	45
A.1	Gate Fabrication Illustration	65
A.2	Wirebonding a Chip	67

List of Figures

B.1	Loading a DXF Design File	69
B.2	Electric Potential Calculation	70
B.3	KWANT : Tight Binding Model and Band Structure	70
B.4	KWANT : Transport Simulation	71

Acknowledgements

As I write this final section of my thesis on a rainy Vancouver evening with a cup of ‘Belfast Brew’ in hand, I can’t help but reminisce on this chapter of life as it comes to an end. I have spent the last seven years at the University of British Columbia, where the last three in the Quantum Devices Group have been a particular highlight. I must start by thanking all current and former members of the group. Much work is required to study quantum dots, and none of my work would have been possible without all the effort that has been put into creating an educational and thought-provoking lab environment.

Of course, my first personal thanks goes to my supervisor, Professor Joshua Folk. Over the last three years, his ability to explain tricky concepts, patience to ensure my understanding and attention to detail has made me a better physicist. One of many skills that I will take with me is understanding when I do and do not understand.

Dr. Silvia Lüscher: Much have I learnt from Silvia on mesoscopic physics and the art of fabrication. In meetings, Silvia’s insights offered alternate paths to a solution. These insights were a reminder to explore all options before settling on an answer. Also, her Swiss chocolate recommendation (‘Ragusa’) is excellent.

Dr. Timothy Child: A senior PhD student who was my mentor during my first year in the group. We worked together closely in my second year. Many long days were spent together being serenaded by the pulse tube. It didn’t take long for us to become friends. Joined by a genuine passion for learning and adventure, our many discussions and deliberations were not only of great academic but also personal interest. I look forward to staying in touch and perhaps trying caving in Slovenia.

Acknowledgements

Vahid Mohaved: A PhD student who joined in my final year here. Our love for coffee brought us together on many Tim Horton’s trips where we discussed physics and more.

Elena Cornick: A Ph.D. student who joined me in my final half-year here. Although we only had a short cross-over, we worked efficiently, and Elena’s theoretical insights were a welcome challenge to my ‘tennis ball’ model of electrons.

Lily Watt: An undergraduate student who worked on perfecting our ohmic recipe. I always enjoyed the insightful questions and wish her the best as president of UBCQ.

Raveel Tejani: An undergraduate who tackled the brave task of developing ‘master-slave’ functionality for our measuring instruments. Our lunch walks for pizza slices and discussions on climbing were enjoyable breaks from weeks of confusing measurements.

Dr. Yigal Meir, Dr. Eran Sela, and Dr. Andrew Mitchell: Our theory collaborators for their expertise and understanding of how to translate their theoretical frameworks onto our experiments.

Our ‘Quantropy’ collaborators at ETH Zurich (Klauss Ensslin and Thomas Ihn’s group), and Université Paris-Saclay (Frederic Pierre’s group), thank you for organising the Quantropy conferences over the past three years. The wide range of disciplines and shared goals fostered fruitful conversations. Witnessing the birth and debate of new experimental ideas was remarkable.

Diego, Mason, Pearce and Luke: My best friends from University and back home in Ireland. We have all moved to different cities, but our friendships remain strong. I always look forward to our calls for fresh perspectives and annual, sometimes bi-annual, meetups for a beer or three. Whether we are discussing the details of heat pumps or walking 60 km for a fish and chips, our adventures are always a pleasure.

Čeňka: My sister, we have grown up greatly over the past few years, although it seems that distance has brought us closer. I love all that we do together, from our debates to our dance-offs; I look forward to being closer to home in the future.

Jana and Peter: My parents, it goes without saying that you influence

Acknowledgements

much of who I am. I always look forward to our weekly catchups, whether they are long or short; they keep me rooted. They say that home is where you are known the most and appreciated the least. But not in this case. You were my first educators and now my best friends.

Olivia: My fiancée and future wife. Little did I know that seven years ago, when I decided to cross the Atlantic, I would find a life partner. We are there for each other, for the big and small, the highs and lows. From our protein bar assembly line to our 14 hour hikes and evening tea time, who knows what our next chapter will hold. I look forward to it with eager anticipation.

Dedication

Be Bright,

Be Brief,

Be Off.

—My Irish granny, Eileen Drayne

Chapter 1

Introduction

“In mesoscopic physics, you really need to build up intuition, because it is not the world you know.”

CARLO BEENAKKER [1]

1.1 Context

Mesoscopic physics is in the domain of condensed matter physics with system scale sizes between nanometre and micrometre. Mesoscopic systems unveil a rich zoo of quantum phenomena and material properties. One of the initial measurements of a mesoscopic system studied the conductance through a quantum wire [2], [3]. Classically, the conductance is expected to be proportional to the width of the wire. However, as the width varies, it was found that a quantum wire exhibits steps at integer conductance values. Each step in conductance is the result of an additional 1D-sub-band that contributes to the transport. Another milestone in the field was the measurement of Coulomb blockade oscillations in the conductance measured across a quantum dot [4]. In this experiment, a small isolated island of electrons was connected to two baths of electrons through tunnel barriers. The island’s small size results in charge quantisation and significant spacing between orbital energy levels, forming an ‘artificial atom’. The benefits of this system come from a high degree of tunability and control. The relevant scales that allow human control over this ‘artificial atom’ are illustrated in Fig. 1.1. The scope of mesoscopic physics is continually expanding, with ongoing developments in new materials [5], measurement methods [6], and device architectures [7], [8].

1.1. Context

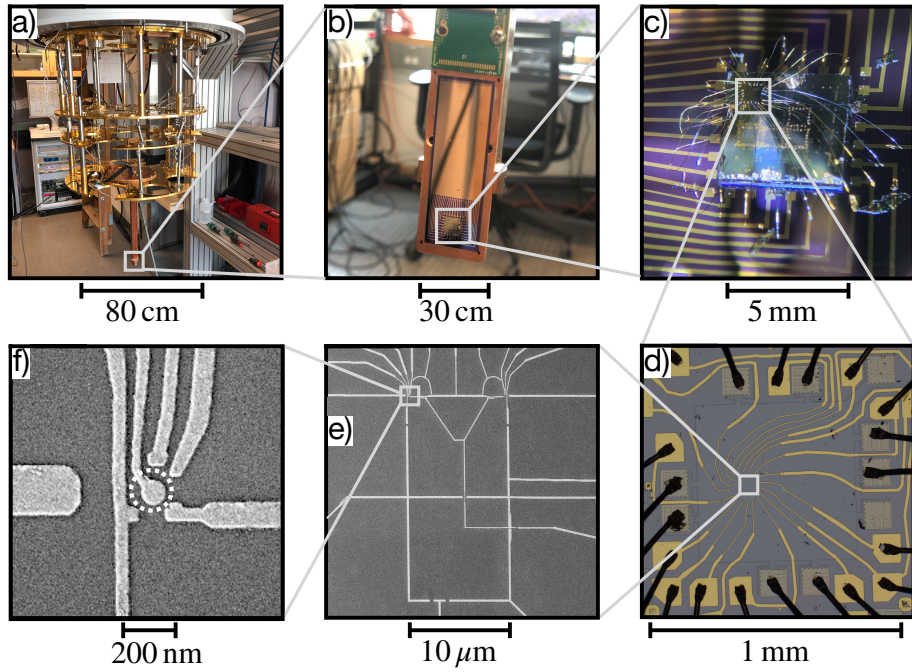


Figure 1.1: Illustrating the relationships from macroscopic to nanoscale to demonstrate the tunability of quantum devices. (a) Photograph of the Au-plated cold plates within a dilution refrigerator. The lowest plate, known as the mixing chamber, can reach temperatures of 8 mK. (b) Photograph of the Si chip carrier, onto which the heterostructure is attached. (c) An optical microscope image shows the heterostructure attached to the chip carrier. Thin Al wire bonds connect the quantum device to the fridge wires. (d) Optical microscope image of a single mesa on the heterostructure. A mesa is an isolated area of the heterostructure where new designs are fabricated. The black lines around the outside are wire bonds and the bright Au are thick (100 nm) ‘outer gates’ which connect to thin (10 nm) ‘inner gates’. (e) Scanning electron micrograph (SEM) of the inner gates. The mean free path of the electrons is of order 3 μm . (f) SEM image of the quantum dot. An isolated puddle of electrons with a total occupation between 0 and 10 is engineered by carefully tuning the voltages on the inner gates.

Theorists and experimentalists enjoy a symbiotic relationship in mesoscopic physics. Experiments validate established theories, while theorists are

1.1. Context

tasked with modelling surprising and repeatable phenomena discovered in experiments. Notable examples of successful experiments validating theory include the investigation of Wigner crystals [9], isolation of graphene [10], and measurement of the charge of quasiparticles in the fractional quantum Hall effect [11]. Conversely, instances of unexpected experimental findings that prompted theoretical inquiry include integer quantum Hall effect [12], anomalous Landau quantisation [13], and superconductivity in twisted double bilayer graphene [8].

This thesis focuses on a phenomenon initially discovered through experimental observation, prompting theorists to develop a new model capable of predicting the striking behaviour observed in measurements. The ‘Kondo effect’, first discovered in impure bulk metals in the 1930s [14] and explained later in the 1960s [15], has seen significant interest in the field of quantum devices. These devices offer high tunability and control, allowing for testing theoretical predictions [16]. The Kondo effect in quantum devices involves a net spin (odd number of electrons) in a quantum dot that is strongly coupled to two electron reservoirs (leads). Virtual tunnel events through the quantum dot, with possible spin flips, lead to a correlated state called the Kondo singlet. The Kondo effect can be seen in the enhanced conductance between Coulomb peaks with decreasing temperature. This conductance approaches the unitary limit, where the transmission probability through the quantum dot is one [17]–[19]. This is a remarkable effect as the tunnel barriers into the quantum dot each have a transmission probability less than one. More recent experiments have explored exotic regimes of the Kondo effect. For example, Kondo effect in graphene [20], Kondo lattices which are used to study quantum criticality [21], multi-channel Kondo which could lead to non-Fermi liquid behaviour [22]–[24], and the novel topological Kondo effect which could demonstrate the non-local quantum dynamics of Majorana fermions [25]–[27].

Nevertheless, there remains considerable potential for further insights by extending the scope of the initial, seemingly ‘simple’ measurements on the Kondo effect into new parameter regimes. In this thesis, we develop and test a method for measuring the Kondo effect with weaker coupling

1.2. Outline

than previously explored. This regime is rarely explored as the conductance enhancement from Kondo is small, and cannot be reliably extracted with a conductance measurement only. Interestingly, a recent measurement of entropy in this regime found a disagreement with theoretical predictions [28]. Hence, this measurement of conductance taken in a similar regime could illuminate potential reasons for the discrepancy.

1.2 Outline

Chapter 2 provides an overview of quantum devices. The chip material (GaAs/AlGaAs heterostructure) is introduced and how the metal gates on top of the chip are used to engineer quantum structures such as quantum point contacts and quantum dots. Additionally, measurements of conductance and occupation through a quantum dot are described.

Chapter 3 introduces the Kondo effect in bulk materials and quantum dots. It includes a measurement demonstrating the large conductance enhancement caused by the Kondo effect in the ‘Kondo regime’, highlighting the differences from the regime discussed in the subsequent Chapter 4.

Chapter 4 demonstrates a method to measure the conductance enhancement from the Kondo effect with weaker coupling. Various dot configurations are tested, with results compared to the Numerical Renormalisation Group (NRG) theory.

Chapter 5 consolidates the main findings from Chapter 4, and outlines future directions for this research.

Chapter 2

Device Background

“If I have seen further it is by standing on the shoulders of Giants.”

ISAAC NEWTON [29]

2.1 Introduction

Before describing the measurements that are the focus of this thesis, it is important to first introduce the devices used to engineer interesting states and the tools used to measure them. As an overview, the chip is a GaAs/AlGaAs heterostructure; the precise layering of the semiconductors form a two-dimensional electron gas (2DEG) around 50-100 nm below the surface of the heterostructure. Voltages applied to patterned metallic gates on top of the heterostructure tune the potential landscape in the 2DEG, controlling where the electrons can go. This tunability allows for forming quantum structures such as quantum point contacts (QPCs) and quantum dots. Ohmic contacts are used to contact the 2DEG to measure transport through such structures.

2.2 Two Dimensional Electron Gas (2DEG)

The quantum point contacts (QPCs) and quantum dots described later in this thesis are engineered in a two-dimensional electron gas (2DEG). A 2DEG can be thought of as a two-dimensional plane of electrons. The electrons can move freely along the x and y directions but are tightly confined in the z-direction. The 2DEGs in this thesis are realised in a GaAs/AlGaAs heterostructure illustrated in Fig. 2.1. A semiconductor heterostructure

2.2. Two Dimensional Electron Gas (2DEG)

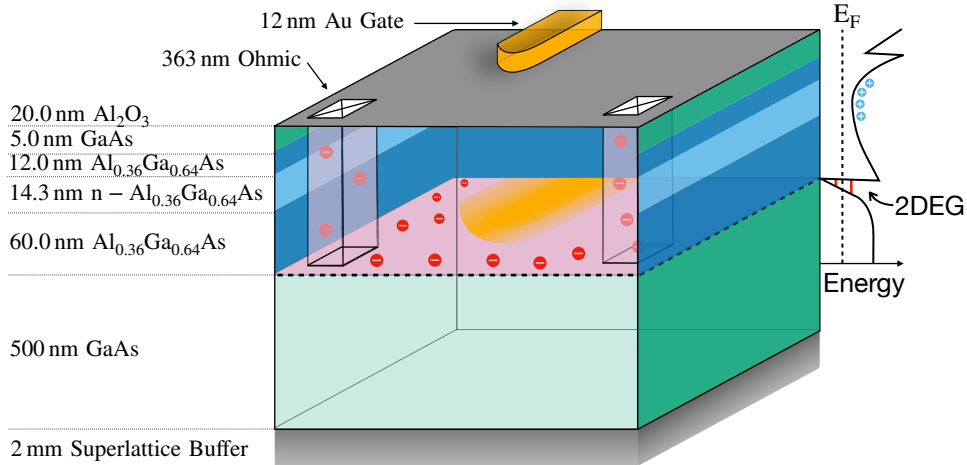


Figure 2.1: Illustration of a GaAs/AlGaAs heterostructure. At the boundary between GaAs and AlGaAs, a two-dimensional electron gas (2DEG) is formed. A 2DEG can be thought of as a two-dimensional plane of electrons that can move freely along the x and y directions but are tightly confined in the z-direction. Ohmic contacts are made by annealing Ni-Au-Ge; the metal diffuses through the heterostructure, making contact with the 2DEG. Ohmic contacts are used to measure conductance through the 2DEG. Voltages are applied to gates to control the potential in the 2DEG, forming quantum point contacts (QPCs) or quantum dots. A negative (positive) voltage on the gate repels (attracts) the electrons.

refers to a material system composed of two or more semiconductor materials with different bandgaps or lattice constants that are layered together. These layers are typically grown on top of each other using techniques such as molecular beam epitaxy (MBE). The heterostructures in this thesis are grown by Michael Manfra's lab at Purdue University [30].

Two characteristics of this heterostructure give rise to a 2DEG. Firstly, $\text{Al}_x\text{Ga}_{1-x}\text{As}$ has a tunable bandgap ranging from 1.42 - 2.16 eV [31] whilst GaAs has a bandgap of 1.42 eV. Secondly, an n-type dopant layer is sandwiched between the $\text{Al}_x\text{Ga}_{1-x}\text{As}$ layers [32]. The smaller bandgap of GaAs allows the electrons from the donor atoms in the dopant layer to drop into the GaAs conduction band, resulting in a triangular potential well (Fig. 2.1).

2.3. Quantum Point Contact (QPC)

This triangular well contains multiple energy levels. The Fermi energy lies between the first and second energy level, so that only the first energy level is occupied. As the second energy level is ~ 150 meV above the first, it will remain unoccupied as this energy gap is much greater than measurement temperatures 500 mK ≈ 43 μ eV and source-drain bias 100 μ eV. Hence, the electron gas is considered two dimensional [33].

Efforts are made to keep the heterostructure and 2DEG clean and defect-free. A 7 nm cap of GaAs is placed on top of the heterostructure to prevent oxidation. Also, a small lattice mismatch between the GaAs and Al-GaAs [34] layers keeps the number of boundary defects in the 2DEG plane low. The 30 nm AlGaAs buffer layer between the 2DEG and dopants helps prevent defects near the 2DEG plane. The resulting 2DEG has a mobility of $\mu_e = 2.56 \times 10^6$ cm 2 /Vs and electron density $n = 2.42 \times 10^{11}$ cm $^{-2}$

Fabrication details on these devices are described in Appendix A. As an overview, the heterostructure is divided into separate areas with isolated 2DEGs by etching away the top layers of the heterostructure, removing the 2DEG underneath. Contact to the 2DEG is made with ohmic contacts. These are made by annealing a layer of Ni-Au-Ge; the metal diffuses through the heterostructure and forms an electrical connection to the 2DEG. On top of that, an insulating dielectric of 10 nm Al₂O₃ is deposited across the surface of the heterostructure to limit leakage from the metallic gates that are added afterwards [35]. A thin layer (10 nm) of Au is deposited to form the ‘inner gates’. The structure and shape of the inner gates have been carefully designed so that QPCs and quantum dots can be formed in the 2DEG. In the second step, a thick layer (100 nm) of Au is deposited (‘outer gates’) to connect the inner gates to square bond pads. Wire bonds are then made from a chip carrier to the square bond pads to connect the fridge wiring and quantum device.

2.3 Quantum Point Contact (QPC)

In this thesis, a quantum point contact (QPC) is a one-dimensional channel connected to a source and drain lead (Fig. 2.2). A one-dimensional channel

2.3. Quantum Point Contact (QPC)

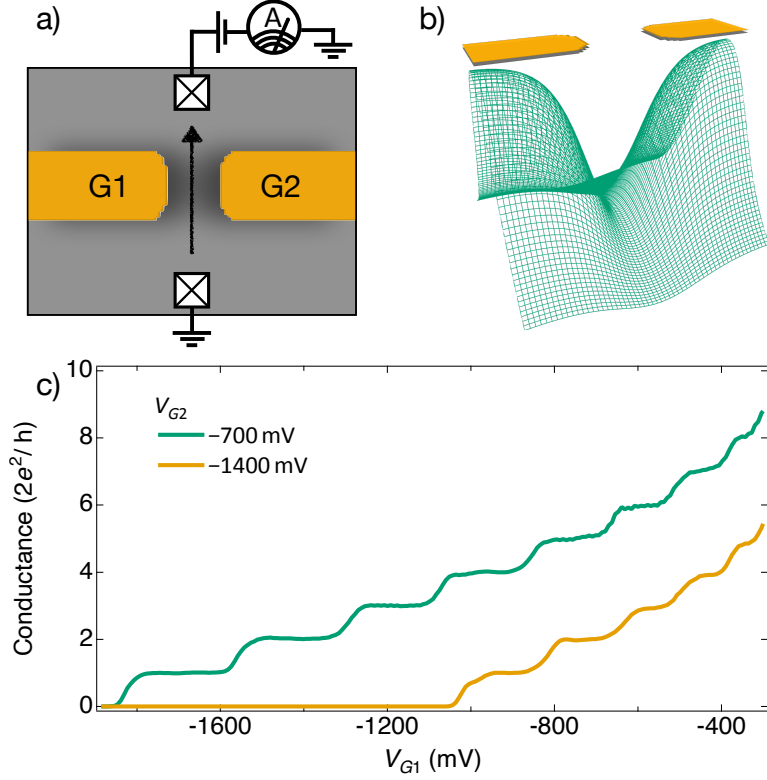


Figure 2.2: (a) Graphic representation from a top-down view of a quantum point contact (QPC). The gold fingers are the metallic gates to which negative voltages can be applied. The grey is where the electrons in the 2DEG can go, depending on the negative voltage applied to the gates. The crossed squares are ohmic contacts to the 2DEG. These contacts allow a bias across the QPC to be applied, so a conductance through the QPC can be measured. (b) Simulation of the electric potential the electrons see in the 2DEG due to the negative voltage applied to the gates [36]. With sufficient negative voltages applied to the gates, the electrons cannot overcome the potential barrier under the gate and flow between the gates. (c) Measurement shows the quantised conductance through a QPC as the voltage on G1 becomes more negative. At sufficiently negative voltages, the potential barrier between the gates is large enough that a measurement will not record any tunnelling events, and the conductance is zero. The pinch-off is shifted from a more negative (green) to a less negative (yellow) value by increasing the negative voltage applied to G2.

2.3. Quantum Point Contact (QPC)

in the 2DEG can be engineered by applying sufficient negative voltage on two metal gates on the surface of the heterostructure with a gap in between. Using the ohmic contacts, a potential bias is applied across the QPC, and a current will flow. The more negative the voltage on the gate, the higher the potential barrier is for the electrons in the 2DEG. A large enough potential barrier can stop the electrons flowing underneath the gate (called ‘depletion’). However, due to the gap between the gates, the electrons can still flow from one side of the QPC to the other. Figure 2.2b shows a simulation of the electric potential in the 2DEGs where the gates are depleted, but electrons can still tunnel between [36]. Further details on this simulation are described in Appendix B. It usually requires a more negative voltage to stop electrons flowing between the gates (called ‘pinch off’). A QPC length is the length of the one-dimensional channel, and the width is the space between gates. In the devices used in this thesis, a QPC can have lengths 50 - 350 nm and widths 100 - 350 nm, depending on its usage.

The electrons are free to move in the y direction, but if the width of the QPC is comparable to the Fermi wavelength, the allowed energy levels are quantised in the x direction. The confining potential in the x direction can be modelled as a parabolic potential as seen in Fig. 2.2b. The allowed 1D energy levels resemble solutions to the harmonic oscillator. Without a magnetic field, each occupied energy level contributes $2e^2/h$ to the conductance. The factor of 2 comes from the spin degeneracy of the electrons, which can be lifted with a magnetic field. When measuring the conductance through a QPC as it is pinched off (Fig. 2.2c), plateaus at integer values of $2e^2/h$ [2] are a signature of the quantised conductance. As the temperature is increased, the plateaus become smeared out. A shorter length of QPC also leads to more narrow plateaus.

In our devices, QPCs are utilised to form tunable tunnel barriers between a quantum dot and a lead (described in the next section) and charge sensors [37], which measure the charge around a quantum dot.

2.4. Quantum Dot

2.4 Quantum Dot

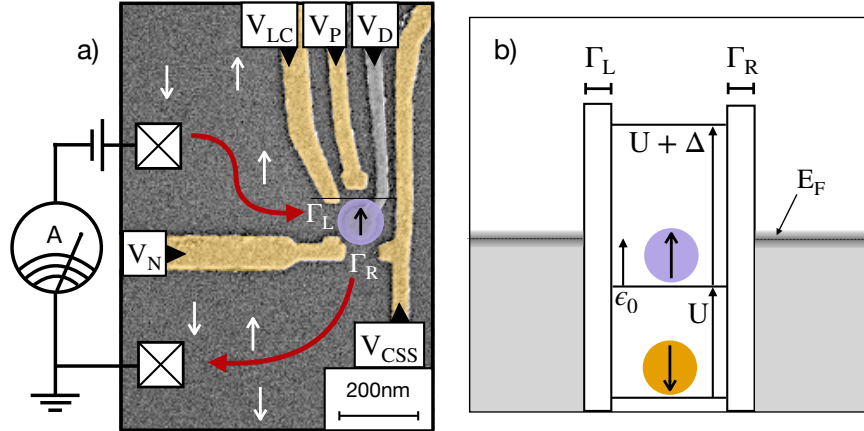


Figure 2.3: (a) SEM image of the gates used to define a quantum dot. The gold-coloured gates indicate sufficient negative potential is applied such that the 2DEG below is depleted. The gates V_P or V_D have the largest effect on dot energy ϵ_0 without changing other energies. The crossed squares are ohmic contacts which contact the 2DEG. A small bias applied to the ohmic contacts allows conductance through the quantum dot to be measured. (b) Coulomb blockade energy diagram showing discrete energy levels in the quantum dot and continuous energy levels in the leads. The grey boxes represent continuous energy levels of the electrons in the leads. The white rectangles represent tunnel barriers into and out of the quantum dot. The tunnelling rate is denoted by the parameter Γ ; the wider (narrower) the barrier, the smaller (larger) the tunnelling rate. The orange circle represents the first electron in the quantum dot with spin down. The second electron (purple) will pair with the first spin-down electron, so the energy required to add the second electron is only the charging energy U . To add the third electron (not currently in the quantum dot), the charging energy U , plus the orbital level spacing energy Δ , is required.

In this thesis, a quantum dot is a zero-dimensional structure. It can be formed by connecting a potential well to source and drain leads through a tunnel barrier [38]. Like a QPC, the potential well is formed by applying negative voltages to gates to confine a small region in the 2DEG. Figure 2.3a

2.4. Quantum Dot

is an example of the gate geometry used for a quantum dot. The tunnel barriers that connect this isolated region in the 2DEG to source and drain leads are formed by QPCs. The first characteristic of quantum dots is the charging energy, U (Fig. 2.3b). This is the energy required to add or remove an electron from the quantum dot due to the Coulomb force. Under certain conditions, the charge in the quantum dot is quantised and equal to Ne , where N is the total number of electrons and e is the charge of a single electron. The two conditions for quantised charge are $R_t \gg h/e^2$ and $U \gg k_B T$. The first condition is the resistance of the tunnel barriers R_t , should be greater than the resistance quantum, $h/e^2 = 25.813 \text{ k}\Omega$. Qualitatively, the tunnel barriers should be large enough so the electron is located in the source or drain leads, or quantum dot. The second condition is that the charging energy, U , should be larger than the system's thermal energy. These conditions lead to a quantised charge in the quantum dot. However, the quantised charge is not a unique feature of quantum dots and is seen in small metallic islands such as Sn particles [39]. The second characteristic of a quantum dot is if the size of the dot is comparable to the de Broglie wavelength, additional contributions to the energy level spacing arise from the orbital level spacing, Δ [38], [40] (Fig. 2.3b). Contributions from orbital level spacing are important when $\Delta \gg k_B T$. Here the energy level spacing is greater than the thermal energy of the system. The simplest model, which combines charging energy and orbital level spacing, is the constant-interaction model [41].

2.4.1 Conductance Through a Quantum Dot

A quantum dot is formed by applying negative voltages to gates which confine a small region in the 2DEG (Fig. 2.3a). Careful gate design is used so that each gate has a primary function, e.g., varying the tunnel barrier or potential well depth. In Fig. 2.3a, V_{LC} is the ‘left coupling’ gate and has the strongest effect on the left tunnel barrier along with V_N . V_N is the ‘nose’ gate and affects both couplings equally. It also has a large effect on the dot energy and can push the location of the electron wave function closer to

2.4. Quantum Dot

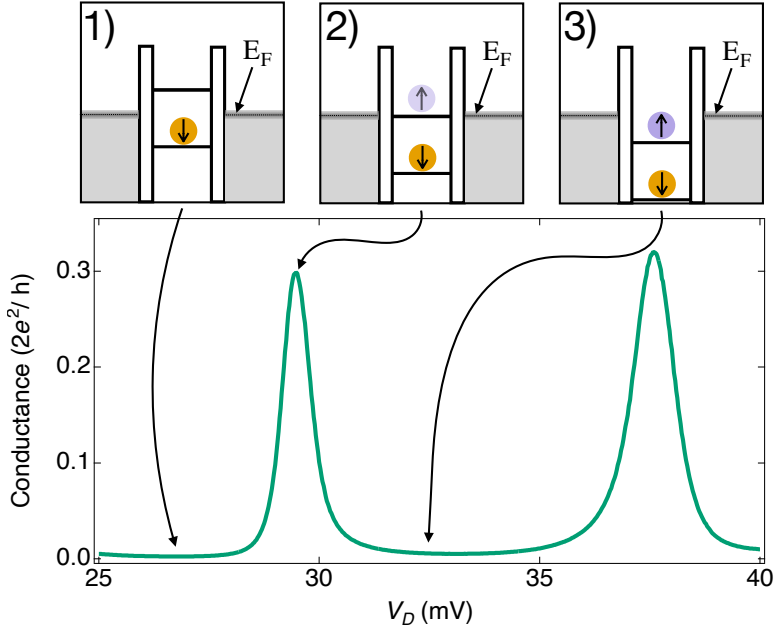


Figure 2.4: Measured conductance through a quantum dot (green trace) as a single electron is added. The corresponding Coulomb blockade energy diagrams show how the energy level of the quantum dot varies. In 1), there is a single electron in the quantum dot (orange dot) and the next available energy level (above the Fermi energy of the source and drain leads) is empty. Here the conductance is zero as no electron in the leads has sufficient energy to tunnel into the quantum dot and off again. In 2), V_D is more positive, lowering the dot energy, ϵ_0 . The dot energy now aligns with the Fermi energy of the source and drain leads. Resonant tunnelling through the quantum dot gives a maximum in measured conductance. On average, there is a fraction of the electron charge in the quantum dot (partial purple dot). In 3), the V_D is made even more positive, and the dot energy ϵ_0 is below the thermal broadening of the electrons in the source and drain leads. The quantum dot is fully occupied (purple dot), and conductance drops to zero.

V_{CSS} . V_{CSS} is the ‘charge sensor spine’. The charge sensor is discussed in the next section, but the proximity of the electron’s wavefunction to V_{CSS} is important for the higher sensitivity of the charge sensor. V_P is the ‘plunger’ gate and primarily controls the dot energy ϵ_0 . By making this gate less

2.4. Quantum Dot

negative, the dot energy decreases or the size of the potential well increases, and at some point, another electron can enter the quantum dot (Fig. 2.4). V_D is the ‘dot’ gate. This gate is operated differently from the other gates as it lies directly above where the electrons in the quantum dot live. This gate is most strongly coupled to the dot energy and is used to add or remove single electrons into the quantum dot with fine control. This gate is usually at positive voltage values to help form a nicely shaped potential well, as negative voltages will form a doughnut-shaped potential.

2.4.2 Charge Sensing a Quantum Dot

A charge sensor is a way to measure changes in the charge in the quantum dot. If correctly tuned, it is very sensitive to the additional charge of an electron that enters a quantum dot [42]–[44]. It is formed by adding a QPC near the quantum dot. The charge sensor is formed using the gate V_{CSQ} , in Fig. 2.5a. Changing the voltage applied to V_{CSQ} allows the QPC to be tuned so that the current is on a steep slope or plateau (Fig. 2.2c). When used as a charge sensor, the QPC is adjusted to be on a steep slope. In this setting, small changes in nearby potentials (x-axis of a QPC trace) show up as large changes in the current measured through the QPC [45]. In Fig. 2.5b, the QPC is set up on a steep slope, and V_D is swept from negative to positive, lowering the dot energy ϵ_0 past the Fermi energy of the leads, so that an electron tunnels into the dot. The background increase in current is due to the capacitive coupling of V_D . As V_D is swept to more positive voltages, the potential in the QPC lowers, and the measured current increases. Once an electron can tunnel into the quantum dot, the extra negative charge of the electron shows up as a small but sharp decrease in current through the QPC, which is called a ‘charge transition’. The derivative of the current can be used to identify charge transitions in large scans where there is a significant change in background current. The steep slope of the charge transition shows up as a large negative spike in the derivative.

2.4. Quantum Dot

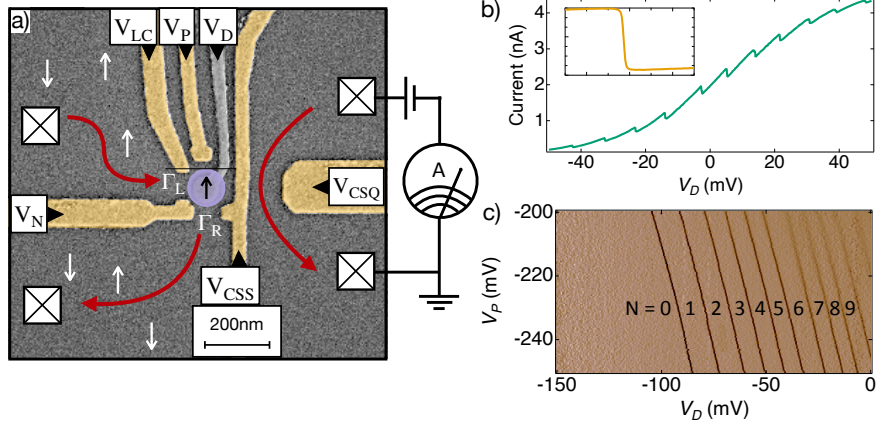


Figure 2.5: (a) SEM image of the gates used to define a quantum dot. The gold-coloured gates indicate sufficient negative potential is applied so that the 2DEG below is depleted. The gates V_P or V_D have the largest effect on dot energy ϵ_0 without changing other energies. The crossed squares are ohmic contacts which contact the 2DEG. V_{CSQ} forms a QPC near the quantum dot. By setting up the QPC on a steep slope between conductance plateaus, the current through the QPC is sensitive to nearby changes in charge. (b) Measured current through the charge sensing QPC. As V_D becomes less negative, the current through the QPC increases. The downward jumps in current result from the negative repulsion from electrons entering the quantum dot (called charge transitions). The inset (yellow) shows a zoomed-in scan over one of these transitions. (c) 2D scan shows how the quantum dot's occupation changes as a function of V_P and V_D . The data is the differentiated current through the charge sensor. The differential of the steep slopes in a charge transition shows up as a sharp peak. This is useful for locating charge transitions when there is a large change in background current.

Figure 2.5c demonstrates how the charge sensor is used to count how many electrons are in the quantum dot. By making V_D more negative and ensuring the tunnel barriers are small enough for electrons to enter the quantum dot, at some point, there will be a final charge transition signalling the last electron. A 2D sweep with different gates on either axis reveals the relative cross-capacitance between each gate on the dot energy ϵ_0 . From

2.5. Determining Electron Temperature

Fig. 2.5c, a -50 mV change on V_D removes ~ 4 electrons, but -50 mV change on V_P only removes ~ 2 electrons.

2.5 Determining Electron Temperature

Charge transitions can be used to count the number of electrons in a quantum dot [46] or determine the relative cross-capacitance between different gates on the dot energy.

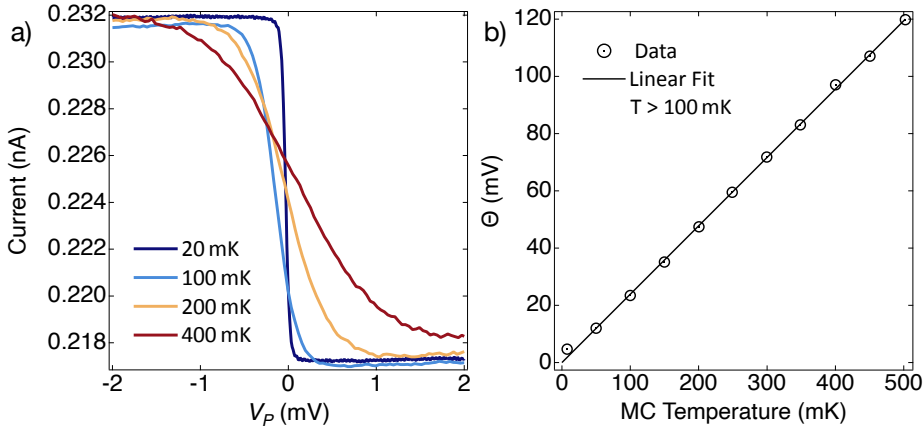


Figure 2.6: (a) Weakly coupled (thermally broadened) charge transition is measured at different fridge temperatures. The broadening of a weakly coupled charge transition is linearly proportional to its temperature. (b) Charge transition's calculated broadening (Θ) at different fridge temperatures. At fridge temperatures $> 100\text{ mK}$, the increase in the charge transition broadening is linear with temperature. This indicates the electrons are well thermalised to the fridge. A linear fit to fridge temperatures $> 100\text{ mK}$ is extrapolated to base temperature to calculate the real temperature of the electrons given the measured broadening. Electron temperature is determined to be 20 mK

However, Fig. 2.6 demonstrates how they can also be used to measure the temperature of electrons in the 2DEG. The broadening of the charge transition depends on the temperature of the system and the size of the tunnel barriers (strength of coupling Γ). When the coupling strength is less

2.5. Determining Electron Temperature

than the thermal energy of the system ($\Gamma/k_B T \ll 1$), the broadening of the charge transition depends only on the temperature of the system. The charge transition is described as thermally broadened or weakly coupled in this regime. The current lineshape of a charge transition in this regime is,

$$I_{CS} = I_{amp} \tanh\left(\frac{V_P - V_{mid}}{2\Theta}\right) + \gamma V_P + I_{const} \quad (2.1)$$

here, I_{CS} is the current through the charge sensor. I_{amp} is the amplitude of the charge transition, V_P is the voltage on the sweep gate used to sweep over the charge transition, V_{mid} is the midpoint of the charge transition. $\Theta = \frac{k_B T}{\alpha e}$ is the thermal broadening in units of gate voltage, $\alpha \equiv \frac{d\epsilon_0}{dV_P}$ is a lever arm that relates changes in a gate voltage to changes in the dot energy ϵ_0 . γ is the cross-capacitance between the sweep gate and the current through the charge sensor. I_{const} is a constant current offset.

The broadening of a weakly coupled charge transition can be used to determine the temperature of the electrons in the 2DEG [47]. Figure 2.6a shows the broadening of charge transitions at a range of temperatures. This broadening is linearly proportional to the temperature ($\Theta \propto T$) of the electrons. At high fridge temperatures, the electrons in the 2DEG are in thermal equilibrium with the fridge. But as the fridge reaches base temperature (8 mK), the electrons in the 2DEG will not be in equilibrium due to poor thermal contact and sources of electrical noise. Also, a source-drain bias across the quantum dot larger than the temperature of electrons can artificially broaden the charge transition (i.e. 1 μ eV = 11.6 mK). Additionally, charge motion in the dopant layer shifts the dot energy up or down, resulting in the charge transition moving left or right in a scan, this leads to artificial broadening. Charge motion can also primarily affect the current through the charge sensor, rather than the dot energy. This charge motion leads to a sudden increase or decrease in current through the charge sensor ('charge jump'). This type of charge motion is only problematic when the jump occurs during a charge transition.

To determine the proportionality constant between the broadening and temperature, charge transitions are measured at a range of fridge tempera-

2.6. Measurement Procedures

tures from 8 - 500 mK. Each charge transition is measured quickly (~ 0.5 s) and repeated many times (~ 300). Any traces with charge jumps near the charge transition are thrown out, and the remaining traces are centred and averaged. The combination of quick scans across the charge transition and averaging, reduces additional broadening from charge motion in the dopant layer. The amount of charge motion in the dopant layer scales between $1/f$ and $1/f^2$ [48]. Each charge transition is then fit using Eq. 2.1, and the calculated Θ is plotted versus the fridge temperature. Figure 2.6b shows a linear fit to Θ between 100 - 500 mK, which is used to determine the proportionality constant. This constant converts the Θ calculated at base temperature into the effective temperature of the electrons in the 2DEG. A base electron temperature of 20 mK was determined in this fridge.

2.6 Measurement Procedures

2.6.1 Cooldown Bias

At room temperature, +200 mV is applied to each of the gates forming the quantum dot and charge sensor (apart from V_D). The positive bias repels the positive charge underneath the gates in the dopant layer. Once the device reaches 10 K, the dopants are frozen in, and the electrons see an effective potential in the 2DEG due to the absence of a positive charge. Cooling with bias has two advantages. Firstly, it reduces the charge noise [49]. Secondly, it reduces the amount of negative potential required on the gates. The effective potential from the positive bias is roughly equal to a negative voltage of equal magnitude when the device is cold (i.e. +200 mV cooldown bias ≈ -200 mV). This is useful as the fine gates can ‘blow up’ (in reality, the metal gates will lift off a little from the heterostructure surface) from high voltages, rendering the device unmeasurable. The fine gates are also sensitive to static discharge, so $1\text{ M}\Omega$ of inline resistance is added to all gates.

2.6. Measurement Procedures

2.6.2 Gate Divider

Fine gate control at large voltages is often required when measuring charge transitions. For example, V_P may require a voltage of -500 mV , but a resolution of 0.001 mV . Digital-to-analog converter (DAC) channels are used to apply voltage on the gates. The DACs have a range of $\pm 10\text{ V}$, with 16-bit resolution. This puts a lower bound on the step size of 0.305 mV ($20\text{ V}/2^{16}$). To achieve a large voltage range with high resolution, two DACs are connected to the same gate. One DAC channel covers a wide voltage range, while the other is used for fine control by adding a voltage divider in line. Voltage dividers between 2 and 100 000 are commonly used to achieve the required resolution (up to 3 nV). All of the voltages in this thesis have been converted to the real voltage applied to the gate (i.e. not the voltage output on the DAC). However, for clarity, only the fine gate may be shown in a figure, even though an additional rough gate applies a large voltage to the same gate.

2.6.3 Virtual Gate

Temperature broadened (weakly coupled) transitions are straightforward to measure and fit. The lineshape is described by an analytic function Eq. 2.1 where the broadening depends on a single parameter, simplifying the fitting routine. In addition, the sharpness of the transition makes visual inspection of the fit trivial. However, the work in this thesis focuses on the gamma broadened (strongly coupled) regime where $\Gamma/k_B T > 1$. The charge transitions in this regime become very spread out, and it can be tricky to inspect the fit quality visually.

One way to tackle this problem is by using a virtual gate. In general, a virtual gate is a name given to a combination of gates that, when varied, change a specific parameter of the quantum dot whilst keeping other parameters constant. The main parameters to control are the dot energy ϵ_0 , left coupling Γ_L , right coupling Γ_R and current through the charge sensor I_{CS} . An example usage would be a virtual gate that controls the left coupling Γ_L only. A combination of V_{LC} and V_P would be used for this virtual gate.

2.6. Measurement Procedures

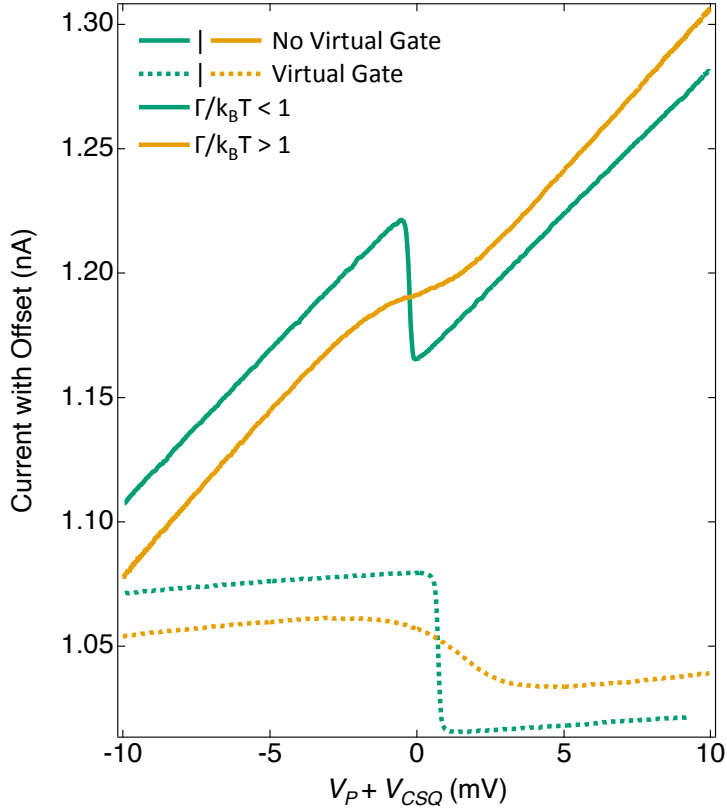


Figure 2.7: Data of a weakly (green) and strongly (yellow) coupled charge transition scanned using a single gate V_P (solid line) and a virtual gate $V_P + V_{CSQ}$ (dashed line). For clarity, the traces have been offset in the current. V_P has a large effect on the dot energy ϵ_0 . However, it also changes the current through the charge sensor I_{CS} due to capacitive coupling. Here, a virtual gate changes the dot energy while keeping the current through the charge sensor constant. This helps to visually identify strongly coupled charge transitions which become very broad. More importantly, the charge sensor stays in the linear regime where changes in the potential are linearly proportional to changes in the current. Note the x-axis is only showing the value of V_P . As V_P is swept negative to positive, V_{CSQ} is swept positive to negative.

2.6. Measurement Procedures

V_{LC} to primarily changed the left coupling Γ_L and V_P to offset any changes to the dot energy ϵ_0 .

In the context of this thesis, only a single type of virtual gate is used. One that changes the dot energy ϵ_0 , but keeps the current through the charge sensor I_{CS} , constant. Figure 2.7 shows the effect of this virtual gate on a weakly coupled ($\Gamma/k_B T < 1$) and strongly coupled ($\Gamma/k_B T > 1$) charge transition. Only two gates (V_P and V_{CSQ}) are used to form this virtual gate. By sweeping V_{CSQ} in the opposite direction of V_P , the cross capacitive effect of V_P on the charge sensor is largely removed.

Chapter 3

Conductance in the Kondo Regime

Ní dhéanfaidh smaoineamh an treabhadh duit.

IRISH PROVERB

3.1 Introduction

This chapter serves as an introduction to the Kondo effect. The history of the Kondo effect began with a measurement that showed a strange behaviour (resistivity minimum with decreasing temperature) in impure gold wires [14]. It took thirty years before Jun Kondo explained this effect, hence the name ‘Kondo effect’ [15]. After another thirty years, advancements in technology revealed the quantum dot as an exciting platform to explore the Kondo effect due to its high degree of in-situ tunability [50].

3.2 Kondo Effect in Bulk Materials

In the 1930s, it was found that the resistivity would surprisingly increase in impure gold wires at low temperatures [14]. This was unexpected as due to electron-phonon scattering, the resistivity should decrease with T^5 before saturating at some non-zero resistivity. Data from the original experiment is plotted in Fig. 3.1 with expected electron-phonon dependence. Over the coming years, it was found that metals with magnetic impurities had a similar behaviour [51].

3.2. Kondo Effect in Bulk Materials

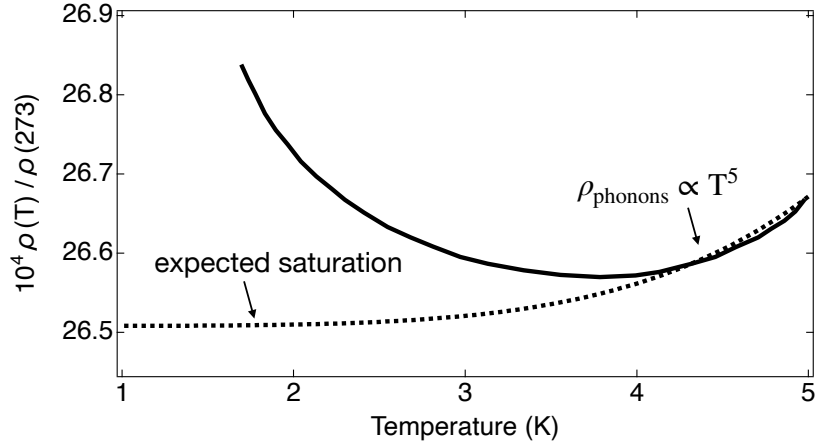


Figure 3.1: Temperature dependence of the resistivity, ρ . In simple metals, the resistivity initially decreases as T^5 due to electron-phonon scattering. However, due to the Kondo effect, the resistivity reaches a minimum before increasing logarithmically with decreasing temperature. The data used for this figure was obtained from [14].

It took until 1964 for a theoretical explanation of the resistivity minimum [15]. Jun Kondo used the s-d model, which couples a metal (non-magnetic, s-band) to a magnetic impurity (unfilled d-level). By looking at the second Born approximation, a logarithmic term appeared, which added a large correction to the resistivity at low T . This contribution comes from a process where spin exchange interactions occur. This work showed that a magnetic impurity at low temperatures can give rise to an alternative scattering process, involving a temporary exchange of spin states between the magnetic impurity and surrounding conduction electrons.

Figure 3.2 illustrates how an exchange of spin states can build a coherent state between the magnetic impurity and the free conduction electrons. It begins with Fig. 3.2a, where conduction electrons surround a magnetic impurity. Figure 3.2b shows a scattering event that may or may not result in the spin-flip of the conduction electron and the magnetic impurity. This leaves the two particles entangled. Continued scattering events between the

3.3. Kondo Effect in Quantum Dots

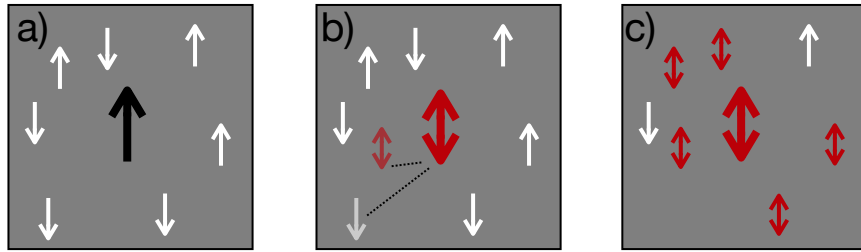


Figure 3.2: (a) A single magnetic impurity (black arrow) is surrounded by conduction electrons (white arrow). (b) Conduction electrons scatter off the magnetic impurity, resulting in a possible spin flip of both particles. This leaves the particles entangled. (c) Continued scattering events build a macroscopic coherent state known as a ‘Kondo singlet’.

magnetic impurity and conduction electrons will result in the macroscopic state shown in Fig. 3.2c. This is known as a ‘Kondo singlet’ or ‘Kondo cloud’. It is found that only a single parameter is needed to describe the low-temperature properties and formation of the Kondo singlet, the Kondo temperature, T_K . Further discussion on the Kondo effect theory is out of this thesis’s scope, but excellent summaries are found here [52]–[54].

3.3 Kondo Effect in Quantum Dots

Until the late 1990s, theorists primarily explored the Kondo effect due to the difficulty of experimentally controlling the Kondo state [51], [52]. However, after advances in quantum dot design, the potential for precise in-situ control was irresistible, and the first measurement of a Kondo singlet was in 1998 [50]. Around this time a scanning tunneling microscope (STM) was also used to study the Kondo effect [55].

In quantum dots, an odd number of electrons results in an unpaired electron that acts as the magnetic impurity in bulk metals. Like bulk metals, the conduction electrons in the 2DEG can interact with the net spin in the quantum dot. The advantage of studying the Kondo effect in quantum dots comes from the in-situ control over the coupling strength, voltage bias, and

3.3. Kondo Effect in Quantum Dots

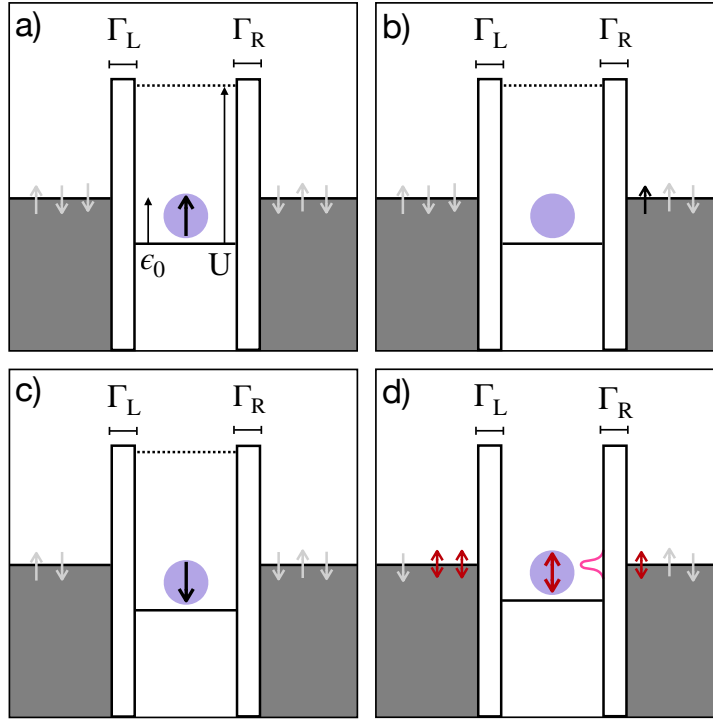


Figure 3.3: Coulomb blockade energy diagram illustrates the formation of a Kondo singlet in a quantum dot. Here, the dot acts as a localised spin. The dark grey represents the continuous energy level of electrons in the leads. The white rectangles represent tunnel barriers between the quantum dot and leads. The rate of tunnelling is denoted by the parameter Γ ; the wider (narrower) the barrier, the smaller (larger) the rate of tunnelling. **(a)** The quantum dot has a one-spin degenerate energy level with dot energy ϵ_0 , occupied by a single electron. The charging energy, U , separates the next energy level. According to Fig. 2.4, zero conductance is expected through the quantum dot. However, **(b,c)** depict a possible virtual tunnelling event. Here, the spin-up electron tunnels out of the dot, and a spin-down electron tunnels into the dot within a short time. **(d)** Many virtual tunnelling events involving possible spin flips lead to a correlated state, the Kondo singlet. This state is pictured as a narrow density of states formed at the Fermi energy of the leads. If a Kondo singlet has been formed, enhanced conductance is measured through the quantum dot, even as the dot energy ϵ_0 is below the energy level of the leads. Note the formation of the Kondo singlet requires an odd number of electrons in the quantum dot.

3.3. Kondo Effect in Quantum Dots

energy level of the magnetic impurity.

The formation of a Kondo singlet in quantum dots is shown in Fig. 3.3. Suppose the dot energy of the quantum dot is far below the Fermi energy of the leads. In that case, the electron is not expected to tunnel out of the dot as it does not have the required energy to reach the available empty energy levels in the leads (Fig. 2.4). However, a second-order tunnelling process can occur resulting in a non-zero conductance, even as the dot energy is below the Fermi energy of the leads. If the electron in the quantum dot tunnels into the leads (Fig. 3.3b) another electron must tunnel into the quantum dot within a timescale limited by Heisenberg's uncertainty principle (Fig. 3.3c). This second-order process can result in a spin flip of the impurity. Many of these virtual tunnelling events will lead to the formation of a singlet state illustrated in Fig. 3.3d. This results in a narrow density of states formed at the Fermi energy of the leads.

Unlike the resistivity increase in bulk metals, the presence of a Kondo singlet leads to enhanced conductance through the quantum dot. Figure 3.4c shows a measurement of conductance at a range of temperatures. At odd occupation, a Kondo singlet is formed and conductance through the quantum dot increases with decreasing temperature. This enhancement of conductance is dependent on a single parameter which sets the energy scale, the Kondo temperature T_K . The Kondo temperature is given by Haldane [56], [57] as,

$$T_K = \frac{\sqrt{\hbar\Gamma U}}{2k_B} e^{\pi\epsilon_0(\epsilon_0+U)/\hbar\Gamma U} \quad (3.1)$$

Here ϵ_0 is the dot energy, U the charging energy and Γ is the coupling of the dot to both source and drain leads, $\Gamma = \Gamma_L + \Gamma_R$. An important realisation from Eq. 3.1, is that the Kondo temperature is not a constant value but is dependent on parameters that can be controlled in an experiment. In Fig. 3.4a, the dot energy is controlled by V_P or V_D and the coupling by V_{LC} , V_N or V_{CSS} . The expression for the Kondo temperature in Eq. 3.1, only holds in the 'Kondo regime'. The Kondo regime is characterised by $\tilde{\epsilon}_0 \ll -0.5$ where $\tilde{\epsilon} \equiv \epsilon_0/\Gamma$. Qualitatively, this regime is satisfied when

3.3. Kondo Effect in Quantum Dots

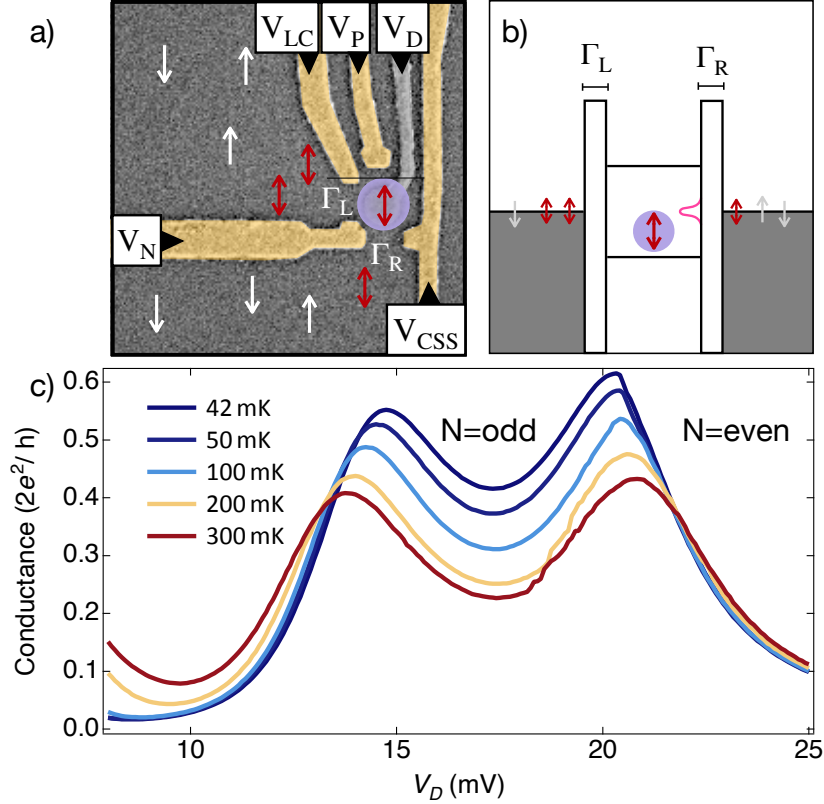


Figure 3.4: (a) SEM image of the gates used to define a quantum dot. The dot contains an odd number of electrons, and the tunnel barriers are tuned to form a Kondo singlet. (b) Coulomb blockade energy diagram picture of a Kondo singlet. As the dot energy falls below the energy level of the leads, there is enhanced conductance due to virtual tunnelling events through the quantum dot. (c) Data showing the temperature dependence of conductance through a quantum dot when a Kondo singlet is formed. In the even occupied sides, conductance decreases as the temperature is lowered. With odd occupation, a Kondo singlet forms, and conductance increases with decreasing temperature.

the full charge of the electron is in the quantum dot. Consequently, as the dot energy is raised so that only a fraction of the electron charge is localised in the quantum dot, this expression for the Kondo temperature

3.3. Kondo Effect in Quantum Dots

breaks down. However, the quantum dot still mainly exhibits a net spin, and Kondo enhancement remains. Importantly, the Kondo temperature increases as the dot energy approaches the Fermi energy of the leads [58], although it may not be exponential in form. This ‘turning on’ of the Kondo effect close to the Fermi energy of the leads is the basis for measurements in the following Chapter 4.

Many early measurements on the Kondo effect in quantum dots used very strong couplings, so the system temperature remained below the Kondo temperature deep into the Kondo regime [17]. Such studies examined temperature dependence of the conductance in the Coulomb blockade valley where the conductance dependence on temperature is non-monotonic and has a minimum at finite temperatures [59]. The Kondo temperature (Eq. 3.1) sets a new many-body scale in the Kondo regime. The Kondo temperature can be used to normalise the conductance such that it is independent of other energy scales Γ , U , and $\tilde{\epsilon}_0$ [16]. This normalisation is given as,

$$G(T) = G_0 \left(\frac{T_K'^2}{T^2 + T_K'^2} \right)^s \quad (3.2)$$

Here $T_K'^2 = T_K / \sqrt{2^{1/s} - 1}$ and $s \approx 0.20$ for a spin 1/2 system in the Kondo regime [58]. The parameter s determines the steepness of the conductance drop with increasing temperature. The one-parameter scaling of the conductance in the Kondo regime is used as one of the demonstrations of the Kondo effect. Other measurements include a zero bias peak in the Coulomb blockade valley [17] and a splitting of this zero bias peak with magnetic field [60].

Other efforts have been made to explore the Kondo effect with less strong coupling. In this regime, the conductance in the middle of the Coulomb blockade valley does not increase with decreasing temperature [58]. However, the dot energy of the quantum dot can be tuned to increase the Kondo temperature. As the dot energy approaches the Fermi energy of the leads, a conductance enhancement due to the Kondo effect can be recovered at sufficiently low system temperatures. The next Chapter 4 will focus on this regime of weaker coupling.

Chapter 4

Occupation Resolved Conductance of the Kondo Effect

Po bitvě je každý generál.

CZECH PROVERB

To my knowledge, the following work in this chapter is the first time that conductance and charge transitions have been simultaneously measured to resolve the conductance enhancement due to the Kondo effect as a function of the quantum dot occupation in an experiment. The conductance enhancement from Kondo is most pronounced when the quantum dot is strongly coupled ($\Gamma/k_B T \gg 1$) to the source and drain leads. Previous measurements of the Kondo effect focus on the conductance enhancement between Coulomb peaks. However, when the coupling is strong, charge transitions broaden and become challenging to convert into the occupation. The following work operates within the narrow spectrum bounded by strong coupling, where the Kondo effect is observable, and weak coupling, where charge transitions are easily measured.

4.1 Introduction

Previous measurements of the Kondo effect in quantum dots study the temperature dependence of conductance between Coulomb peaks. It is in this so-called Kondo regime that the full charge of the electron is in the dot,

4.1. Introduction

so there is a definite net spin, and the theory is well understood [16], [17]. In this regime, the Kondo temperature (Eq. 3.1) sets a new, many-body scale and is used to universally scale the conductance (Eq. 3.2). This one-parameter scaling of conductance in the Kondo regime is used as one of the demonstrations of the Kondo effect. When the coupling between the quantum dot and source and drain leads is reduced, the Kondo temperature drops below the system temperature, and the conductance enhancement is not seen between Coulomb peaks. Only a handful of experiments have studied conductance with less strong coupling [58]. Such studies observed the parameter s from Eq. 3.2 and found that in the Kondo regime (the full charge of the electron is in the dot), s was constant and equal to 0.20. However, as the shoulder of a Coulomb peak was approached ($\tilde{\epsilon}_0 > -0.5$), s varied rapidly. Qualitatively, this regime is entered when the dot energy ϵ_0 approaches the Fermi energy of the leads, and only a fraction of the electron charge is in the dot.

Our aim was to measure the Kondo effect with a coupling strength such that the conductance between Coulomb peaks was zero. This regime, characterised by a relatively small Γ , results in a small Kondo temperature between Coulomb peaks where no conductance enhancement would be measured. However, the Kondo temperature will increase as the dot energy approaches the Fermi energy of the leads (moves towards the shoulder of a Coulomb peak). Hence, for relatively small coupling strengths, the Kondo effect can still be seen as a very small conductance enhancement on the odd occupied shoulder of a Coulomb peak. As the conductance enhancement in this regime is very small, it is insufficient to investigate the Kondo effect with a conductance measurement only, for two reasons. Firstly, entropy shifts the occupation of the quantum dot with temperature. This effect has been taken advantage of in a recently developed entropy measurement technique [6], [28], [61]. This shift in occupation can be ignored when the coupling is strong, and conductance enhancement between Coulomb peaks is large. Secondly, charge motion in the dopant layer can shift the conductance left or right with respect to the gate voltage in a scan. The shifting from charge motion renders it impossible to offset the effects of entropy by

4.2. Occupation Resolved Conductance Method

retroactively shifting conductance. For these two reasons, it is necessary to simultaneously measure a second ‘reference’ signal alongside the conductance. This reference signal can then be used to offset the above effects and allow for comparison of the conductance across multiple temperatures.

We measure the charge in the quantum dot simultaneously with conductance. Assuming a linear relation between the measured change in charge and the real occupation of the quantum dot, the charge transition is converted into an occupation. The occupation is then used to plot the conductance as a function of occupation. A shifting of the conductance maximum to a higher occupation is a signature of the Kondo effect. As the universal scaling of conductance does not hold in this regime, a comparison to theory calculations (described in an upcoming section) is required to verify Kondo enhancement.

4.2 Occupation Resolved Conductance Method

The conductance and charge of the quantum dot are simultaneously measured to investigate the small enhancement of conductance due to the Kondo effect with relatively small coupling. On the hardware side, a simultaneous measurement of the charge and conductance is trivial as two different current amplifiers are simply connected to the device. The first current amplifier measures the conductance through the quantum dot and the other, current through the charge sensor. Each current amplifier is connected to two analog-to-digital converters (ADCs), which sample data points simultaneously. Conductance is measured using a pseudo-lockin technique. Here a DAC channel voltage biases the current amplifier using a $\pm 1 \mu\text{V}$ square wave. The underlying signal is recovered in analysis by multiplying with a sine wave of equal frequency and averaging all the points per square wave cycle. This technique mitigates the effects of bias drift in the current amplifier so that a reliable $1 \mu\text{V}$ source-drain bias is applied across the dot. A constant $100 \mu\text{V}$ DC bias is applied across the charge sensor. Large source-drain bias across the charge sensor can de-phase the Kondo singlet [62], however, a range of $50\text{-}250 \mu\text{V}$ source-drain biases across the charge sensor

4.2. Occupation Resolved Conductance Method

were tested with no significant effect.

It is much trickier to tune the quantum dot into a regime where both the conductance and charge transition can be compared to theory. When weakly coupled ($\Gamma/k_B T \ll 1$), the charge transitions have a sharp drop in current and can be fit analytically using Eq. 2.1. However, a weakly coupled Coulomb peaks amplitude drops with the strength of coupling [40] as,

$$G_0 \propto \frac{\Gamma_L \cdot \Gamma_R}{\Gamma_L + \Gamma_R} \quad (4.1)$$

Here G_0 is the conductance maximum. This decrease in conductance amplitude means that the conductance signal can be lost within the background noise. Additionally, as the Kondo temperature decreases with reduced coupling, the conductance enhancement due to Kondo can become immeasurable.

In a strongly coupled regime ($\Gamma/k_B T \gg 1$), the line shape for a Coulomb peak is given by the Breit-Wigner formula [63]. The conductance is maximum when the dot energy is in line with the Fermi energy of the leads and depends on the coupling as,

$$G_0 \propto \frac{\Gamma_L \cdot \Gamma_R}{(\Gamma_L + \Gamma_R)^2} \quad (4.2)$$

In both weakly and strongly coupled regimes, it is evident that the conductance reaches a maximum when the tunnel barriers are symmetric ($\Gamma_L = \Gamma_R$). Strong coupling also has the added benefit of an increase in Kondo temperature, leading to greater enhanced conductance. However, charge transitions become very broadened and difficult to measure (Fig. 2.7). When strongly coupled, large sweeps in gate voltage are required to cover a range where the quantum dot is fully unoccupied to occupied. This can result in the charge sensor being pushed into a non-linear regime due to the cross-capacitive coupling from the sweep gate. A non-linear relationship between the current through the charge sensor and the addition of charge into the quantum dot makes extraction of dot occupation from the charge transition unreliable. Hence, a virtual gate shown in Fig. 2.7, that keeps the current

4.2. Occupation Resolved Conductance Method

through the charge sensor constant is required. The exact ratio of gates used to form a virtual gate can drastically change the underlying shape of the charge transition, which will be discussed in an upcoming section.

4.2.1 Numerical Renormalisation Group (NRG)

The dot is carefully tuned to a coupling regime where the conductance enhancement due to Kondo is expected, and charge transitions are reliably measured. As previous tests of the Kondo effect are not possible in this regime, a comparison to Numerical Renormalisation Group (NRG) calculations [64] is required. Our theory collaborators (Yigal Meir, Yaakov Kleedorin, and Andrew Mitchell) provide these calculations. Two 2D datasets corresponding to conductance and occupation are received. The columns are energy scaled by Γ (energy/ Γ), so the x-axis is unitless. The rows in the 2D datasets correspond to a different $\Gamma/k_B T$ value. We confirmed with Yaakov that the lineshape does not change if both T and Γ increase together. The lineshape represents the ratio $\Gamma/k_B T$, not Γ or T individually.

To compare NRG to data, $\Gamma/k_B T$ should be reliably determined so the correct row from NRG is used. Then, the correct scaling is applied to convert the NRG into measurement units. Conductance and charge transitions have similar scaling parameters. Amplitude, x-offset and lever arm which scales the NRG x-axis in units of mV. The occupation NRG has extra parameters: a y-offset which comes from the current through the charge sensor, a linear term which comes from the cross-capacitance between the sweep gate and charge sensor, and an occupation-dependent linear term. This occupation-dependent linear term reflects a change in the cross-capacitance as an electron enters the quantum dot. In Fig. 4.5, the charge transition slopes are different between the unoccupied (left) and occupied (right) sides. We argue that the additional charge of an electron in the quantum dot can give rise to such a change in cross-capacitance. Many of these parameters have low cross-correlation when fitting data to NRG, meaning the global minimum of the minimiser is reliably reached. However, this is not true for the parameters $\Gamma/k_B T$ and lever arm. Changes to $\Gamma/k_B T$ can be offset by

4.2. Occupation Resolved Conductance Method

a change in lever arm, and fitting a single trace allowing both parameters ($\Gamma/k_B T$ and lever arm) to vary freely is unreliable.

4.2.2 Conductance Global Fit to NRG

In the temperature broadened regime ($\Gamma/k_B T < 1$), $\Gamma/k_B T$ and lever arm are decoupled as the broadening of the conductance or charge transition is from temperature only. To access the temperature broadened regime from the gamma broadened regime ($\Gamma/k_B T > 1$), the temperature of the fridge is increased until $\Gamma/k_B T \lesssim 1$. Figure 4.1 shows data that is taken at multiple temperature setpoints across this range, so that $\Gamma/k_B T$ and lever arm can be reliably determined. Conductance and charge transitions are simultaneously measured at each temperature. However, only the conductance data is used to determine $\Gamma/k_B T$ and lever arm, as it is generally cleaner. A global fit to the conductance data, including each temperature setpoint, is used in Fig. 4.1a. Here Γ and lever arm are allowed to vary, but held fixed between temperatures, and T is held fixed to the calculated electron temperatures from Fig. 2.6. The other parameters (amplitude and x-offset) used to fit the NRG to conductance data are allowed to vary freely. The fitting range is the full width at 90% the maximum conductance. This removes any bias of picking a ‘good’ fitting range.

4.2.3 Charge Transition Fit to NRG

Each charge transition is fit separately to NRG, where $\Gamma/k_B T$ and lever arm determined from the conductance global fit, are held fixed. All other parameters (amplitude, x-offset, y-offset, linear and occupation-dependent linear) are allowed to vary freely (Fig. 4.1b). The fitting range of the charge transitions is maximised up to, but excluding charge jumps.

4.2. Occupation Resolved Conductance Method

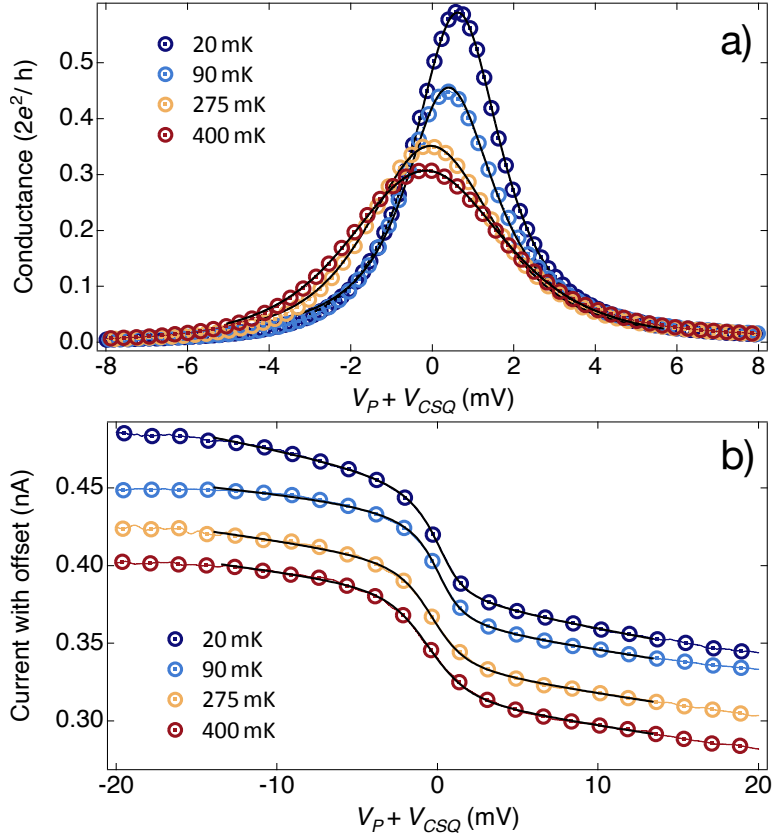


Figure 4.1: (a) Conductance as a single electron enters a strongly coupled ($\Gamma/k_B T > 1$) quantum dot at four different temperatures. The x-location of the conductance maximum has not been shifted and is the original x-location of the measured data. The fits (in grey) are from a global fit to NRG, where the Γ and lever arm parameters are held fixed across all four temperatures. (b) Charge transitions are measured simultaneously with the conductance. Each charge transition is separately fit to NRG, where the Γ and lever arm parameters are held fixed to the values determined from the global fit to conductance.

4.2.4 Determining Occupation

The charge transition cannot be used as a reference to compare with conductance due to changing amplitude and linear terms with changes in dot

4.2. Occupation Resolved Conductance Method

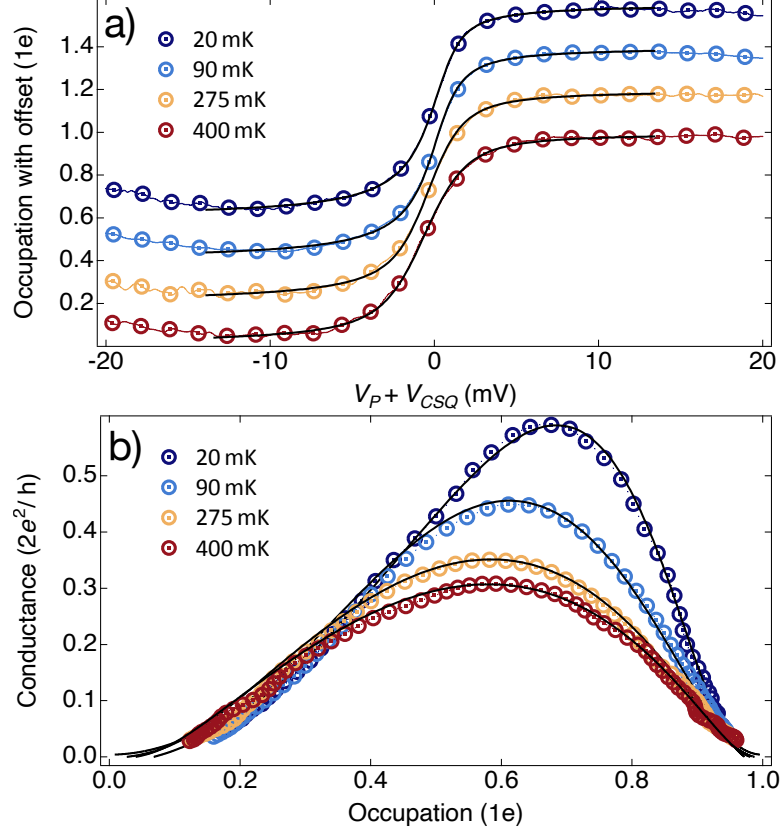


Figure 4.2: (a) Charge transitions are converted to occupation by removing the relevant fit parameters. These are amplitude, current offset, cross-capacitance of virtual gate, and occupation-dependent cross-capacitance. (b) Conductance versus occupation is used to show the enhanced conductance due to Kondo. As temperature decreases, the conductance maximum occurs at greater occupation. The NRG (grey) conductance versus occupation corresponding to the determined $\Gamma/k_B T$ is plotted on top of the data, where good agreement is found at each temperature.

settings. However, charge transitions can be converted into an occupation, allowing for the comparison of conductance enhancement between dot settings. The fit parameters from the NRG fit to the charge transitions are used to remove relevant terms. The current offset (y-offset) and linear term are

4.3. Kondo Effect with Varying Coupling Strength

removed trivially. The occupation-dependent linear term is removed by multiplying this linear term with the correct NRG occupation row corresponding to $\Gamma/k_B T$. Lastly, the charge transition is re-scaled by the amplitude. NRG only has to be shifted by the x-offset and scaled by the lever arm to make a comparison with data (Fig. 4.2a).

4.2.5 Conductance versus Occupation

Plotting conductance versus occupation overcomes the issue of conductance shifting due to entropy or charge motion. Figure 4.2b shows the conductance data plotted against the determined occupation. Conductance enhancement due to Kondo can be seen from a shift of the conductance maximum to occupation greater than 0.5 ($N > 0.5$). This shift in the conductance maximum indicates that even as the dot energy of the quantum dot falls below the energy level of the leads, there is enhanced conductance due to the formation of a Kondo singlet. As the temperature is lowered in Fig. 4.2b, the conductance maximum shifts to higher occupation. This is because the system temperature falls below the Kondo temperature, and the Kondo singlet remains formed. As the conductance and occupation data are fit to different ranges, it is essential to ensure that the conductance and occupation data points plotted against each other correspond to the same gate voltage. The NRG conductance versus occupation in Fig. 4.2b, is the unscaled NRG provided by the theorists corresponding to $\Gamma/k_B T$. There is good agreement between the data and NRG at each temperature.

4.3 Kondo Effect with Varying Coupling Strength

In Fig. 4.2b, the Kondo enhancement dependence on the system's temperature was confirmed. At high temperatures $T > T_K$, there is no Kondo singlet, and so the conductance maximum is near $N = 0.5$. But at low temperatures $T < T_K$, a Kondo singlet is formed, and the conductance maximum shifts to higher occupation $N > 0.5$. This displays the dependence of

4.3. Kondo Effect with Varying Coupling Strength

the Kondo temperature on the dot energy. The Kondo temperature rises as the dot energy gets close to the leads. However, the Kondo temperature also depends on the coupling strength between the quantum dot and leads (Eq. 3.1). As strongly coupled quantum dots have larger Kondo temperatures, the conductance maximum is expected to occur at higher occupation than in weakly coupled quantum dots.

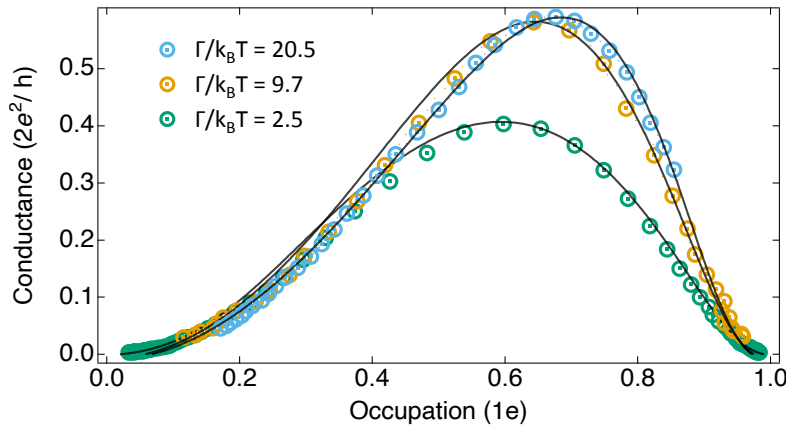


Figure 4.3: Conductance versus occupation in a weak (green) and strong (blue) coupling regime. Each trace is taken at 20 mK. The coupling strength $\Gamma/k_B T$ was determined from a global fit to multiple temperatures. The NRG (grey) conductance versus occupation corresponding to the determined $\Gamma/k_B T$ is plotted on top of the data. Good agreement is found at each coupling strength.

Figure 4.3 shows 20 mK traces of conductance versus occupation at three different coupling strengths. $\Gamma/k_B T$ is determined using the fitting routine described previously and is used to plot the corresponding NRG alongside the data. Expectedly, the more strongly coupled data shows a greater shift in the conductance maximum to higher occupation. Good agreement with NRG is observed at each coupling.

4.4. Kondo Effect with Varying Charge Sensor Current

4.4 Kondo Effect with Varying Charge Sensor Current

This new method of plotting conductance versus occupation not only requires a reliable determination of $\Gamma/k_B T$ and lever arm from conductance data, but also clean charge transitions that can be converted into an occupation. The shape of the charge transition can vary depending on the choice of virtual gate and the charge sensor QPC setpoint. In the next section, different current setpoints of the charge sensor QPC are measured and the resulting conductance versus occupation is tested for agreement with NRG.

4.4.1 Varying Charge Transition

Figure 4.4 shows a charge sensor trace (green) and the resulting charge transition (yellow) at a range of current setpoints through the charge sensor. The current (y-axis) has not been scaled differently between the charge sensor trace and charge transitions. However, the sweep gate (x-axis) of the charge sensor and charge transitions are different. The charge transition sweep gate axis has been scaled for clarity.

The shape of the charge transition varies significantly as the current setpoint through the charge sensor changes. Typically, the charge sensor is set to its steepest slope where the derivative is the largest. Here, the charge sensor is most sensitive as small changes in the potential result in large changes in the current and the resulting amplitude of the charge transition is greatest. However, charge transitions can be measured at any current setpoint through the charge sensor. As long as the change in current through the charge sensor is linear with respect to the change in voltage. This can be achieved with a virtual gate, which keeps the current through the charge sensor constant. Yet, at each charge sensor current setpoint, the charge transition slopes vary differently on the unoccupied and occupied sides. Comparing the slopes on the unoccupied (left) side, at low currents, they point downwards, then point upwards with increasing current, and then point downwards again at the highest current setpoint. It is important to

4.4. Kondo Effect with Varying Charge Sensor Current

show that the conduction versus occupation agrees with NRG, irrespective of the current setpoint through the charge sensor. Otherwise, it may be possible to ‘pick’ a current setpoint through the charges sensor that either shows or does not show agreement with NRG. This would render the method unreliable.

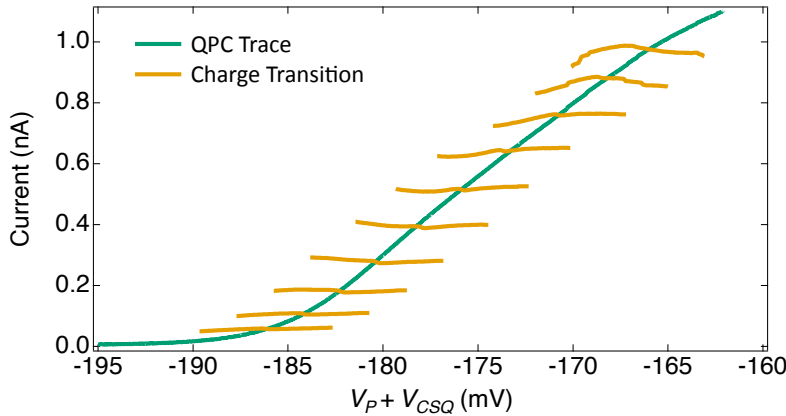


Figure 4.4: Current through the charge sensor (green) from pinch-off to the start of the first conductance plateau. Corresponding charge transition (yellow) at each current setpoint through the charge sensor. Note the x-axis is different between the underlying charge sensor trace and charge transitions. The charge transitions x-axis has been scaled the same amount for clarity. The charge transitions vary dramatically as the current through the charge sensor is changed. The left and right slopes curve upwards, downwards, in the same direction, or opposite each other.

4.4.2 Conductance versus Occupation

Figure 4.5a shows charge transitions taken at 20 mK for three different current setpoints through the charge sensor. For clarity, each charge transition has been offset in the current. The shape of the charge transition clearly depends on the current through the charge sensor. The unoccupied (left) side of the high current (blue) charge transition slopes down, whilst the low current (green) charge transition slopes upwards. This suggests that the op-

4.4. Kondo Effect with Varying Charge Sensor Current

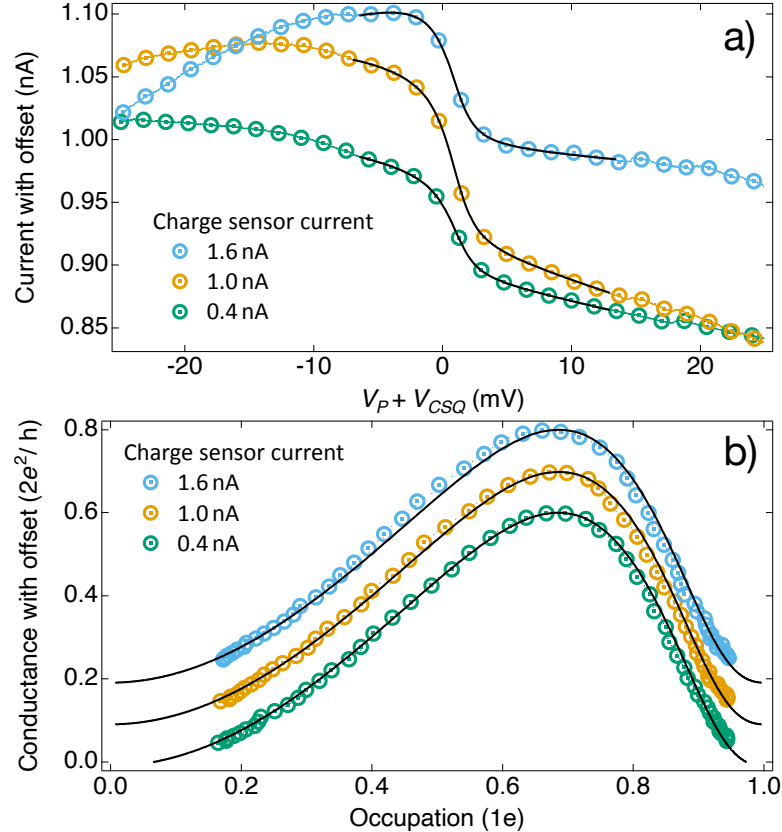


Figure 4.5: (a) Charge transitions are measured with high (blue) and low (green) current through the charge sensor. For clarity, the transitions are offset in the current. The x-axis uses the same virtual gate for each charge transition. The slopes on either side of the charge transitions vary with the current through the charge sensor, suggesting the best virtual gate also changes. (b) Conductance versus occupation ($\Gamma/k_B T = 21$) at different current setpoints through the charge sensor. The traces are offset for clarity. Each trace is taken at 20 mK. The coupling strength $\Gamma/k_B T$ was determined from a global fit to conductance at multiple temperatures. The NRG (grey) conductance versus occupation, corresponding to the determined $\Gamma/k_B T$, is plotted on top of the data. Good agreement is found at each current setpoint.

4.5. Kondo Effect with Varying Coupling Symmetry

timal virtual gate to keep the charge sensor current constant also changes. At each current setpoint, conductance was simultaneously measured at a range of temperatures. A global fit to the conductance was used to determine $\Gamma/k_B T$ and lever arm. Each charge transition was converted into an occupation, and the conductance versus occupation is plotted with a comparison to NRG (Fig. 4.5b). For clarity, the conductance versus occupation traces have each been offset by $0.1 2e^2/h$. Excellent agreement between data and NRG is found at each current setpoint.

4.5 Kondo Effect with Varying Coupling Symmetry

All previous conductance data shown in this thesis was taken with symmetric coupling ($\Gamma_R = \Gamma_L$). Previous measurements of the Kondo effect also tune the quantum dot to be symmetrically coupled with the source and drain leads. However, some experimental studies have investigated the Kondo effect with asymmetric coupling ($\Gamma_R \neq \Gamma_L$) [65]. It was found that the characteristic zero bias peak between Coulomb peaks shifted to a nonzero bias. However, this effect would require a strong energy dependence of the tunnel barriers (i.e., $\Gamma = \Gamma(E)$) in a NRG calculation, which is not assumed in our current NRG calculations. Hence, a measurement of conductance with nonzero bias cannot be currently compared to NRG. Although we may not quantitatively corroborate these previous findings, exploring coupling symmetry is interesting as it effectively tests how the Kondo enhancement varies when a quantum dot is coupled to two leads (symmetric case) versus a single lead (asymmetric case). In practice, the limit of a single lead regime cannot be reached, as conductance will not be measured through the quantum dot.

4.5.1 Symmetric to Asymmetric Coupling

The width of a strongly coupled Coulomb peak is controlled by Γ . Where Γ is the sum of the individual tunnelling rates, $\Gamma = \Gamma_L + \Gamma_R$. The conductance amplitude in both the weakly (Eq. 4.1) and strongly (Eq. 4.2) coupled

4.5. Kondo Effect with Varying Coupling Symmetry

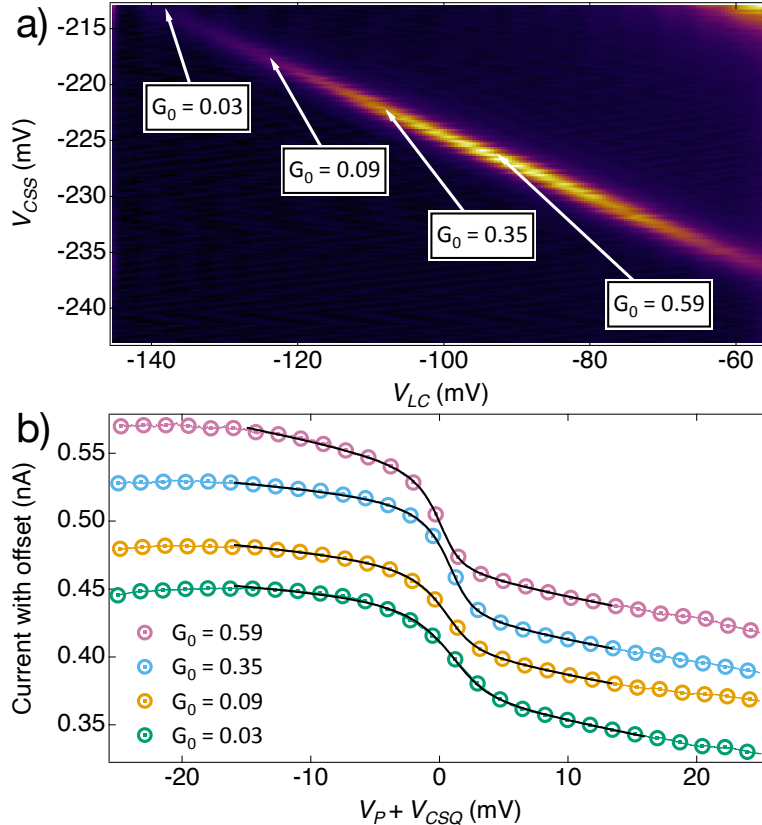


Figure 4.6: (a) 2D scan of conductance through the quantum dot varying the two coupling gates V_{CSS} , and V_{LC} . In the top left, the dot is more coupled to the right lead than the left as V_{LC} is made more negative. In the middle of the scan (where the conductance is maximum), the coupling is symmetric $\Gamma_R = \Gamma_L$ (b) Charge transitions measured with different ratios of coupling between the two leads in the dot. $G_0 = 0.59$ is symmetric coupling (pink), $G_0 = 0.03$ is asymmetric coupling (green). Charge transitions were measured with roughly the same current setpoint through the charge sensor (~ 0.4 nA), but for clarity, they have been offset in the current. The x-axis uses the same virtual gate for each charge transition.

regimes depend on Γ . Hence, the conductance amplitude can be used as a marker of how asymmetrically coupled the quantum dot is to the leads.

4.5. Kondo Effect with Varying Coupling Symmetry

To vary the coupling symmetry in a quantum dot, a 2D scan measuring the conductance with gates that control a separate coupling on each axis is used. In Fig. 4.6a, V_{CSS} (y-axis) mainly controls Γ_R , and V_{LC} (x-axis) mainly controls Γ_L . Four points are picked from symmetric coupling (middle of scan) to asymmetric coupling (top left of scan), where the dot becomes more strongly coupled to the right lead.

Charge transitions were simultaneously measured so that conductance versus occupation could be compared with the corresponding NRG. Charge transitions for each coupling setpoint were measured with $\sim 0.4\text{ nA}$ through the charge sensor (Fig. 4.6b). Each charge transition did not have charge jumps near the transition and was deemed a reliable measure of the occupation. Interestingly, the asymmetrically coupled transition (green) is more broadened than the symmetrically coupled transition (pink). $\Gamma/k_B T$ determined from the global fit to conductance varied from 20.5 for symmetric coupling to 26.0 for asymmetric coupling. However, a global fit to the charge transitions finds 19.6 for symmetric coupling and 45.0 for asymmetric coupling (Table 4.1). This discrepancy between the $\Gamma/k_B T$ value determined from the global fits to conductance and charge transitions is surprising. Conversations with our theorist collaborators suggest that NRG only depends on the overall Γ , and not the ratio between Γ_L and Γ_R .

$G_0 (2e^2/h)$	$\Gamma/k_B T$ from Global Fit	
	Conductance Fit	Charge Transition Fit
0.59	20.5	19.6
0.35	22.0	21.6
0.09	24.4	30.9
0.03	26.0	45.0

Table 4.1: $\Gamma/k_B T$ determined from a global fit to conductance and separately a global fit to charge transitions at different ratios of coupling symmetry. At symmetric coupling ($G_0 = 0.59$), the determined $\Gamma/k_B T$ from conductance and charge transitions are similar. However, at asymmetric coupling ($G_0 = 0.03$), the $\Gamma/k_B T$ from a global fit to charge transitions is much greater than from a global fit to conductance.

4.5. Kondo Effect with Varying Coupling Symmetry

4.5.2 Conductance versus Occupation

Figure 4.7a shows conductance versus occupation taken at 20 mK at the four different ratios of coupling symmetry found in Fig. 4.6a. There is good agreement with NRG in the symmetric coupling (pink). However, as the coupling becomes more asymmetric, the conductance amplitude decreases (Eq. 4.2), and agreement with NRG is difficult to determine. Hence, for clarity, Fig. 4.7b shows the same data with an added scaled and offset. The corresponding NRG was also scaled and offset the same as the data. A disagreement between asymmetric coupling (green) data and NRG becomes much clearer. When asymmetrically coupled, the conductance maximum of the data is shifted to the right of the NRG. This suggests the $\Gamma/k_B T$ determined from the global fit to conductance is lower than expected. This discrepancy with NRG is surprising as conversations with our theorist collaborators suggest that NRG only depends on the overall Γ , and not the ratio between Γ_L and Γ_R .

Previous experiments have investigated the use of a charge sensor as a noise source to de-phase the Kondo singlet [62]. In these studies, the bias across the charge sensor was 1200 μ V, twelve times the bias that is used for the charge sensor in this thesis (100 μ V) and the suppression of the measured conductance was $\sim 6\%$. A more recent theoretical study found that for weak coupling between the charge sensor and quantum dot, the spectral weight of the Kondo resonance is reduced, leading to a suppression of the conductance. However, the width of the resonance is not affected, suggesting the absence of dephasing [66]. Although this de-phasing mechanism could result in the conductance maximum being shifted to a lower occupation, it would not explain a shift to a higher occupation or the dependence on symmetric coupling.

Instead of a change in the shape or location of the conductance, it is possible the charge transition behaves differently between coupling symmetries. Numerous studies have investigated the tunnelling rates onto and off the quantum dot [67]–[69], with differing barrier symmetries [70], [71]. However, these studies required the source-drain bias to be larger than the

4.5. Kondo Effect with Varying Coupling Symmetry

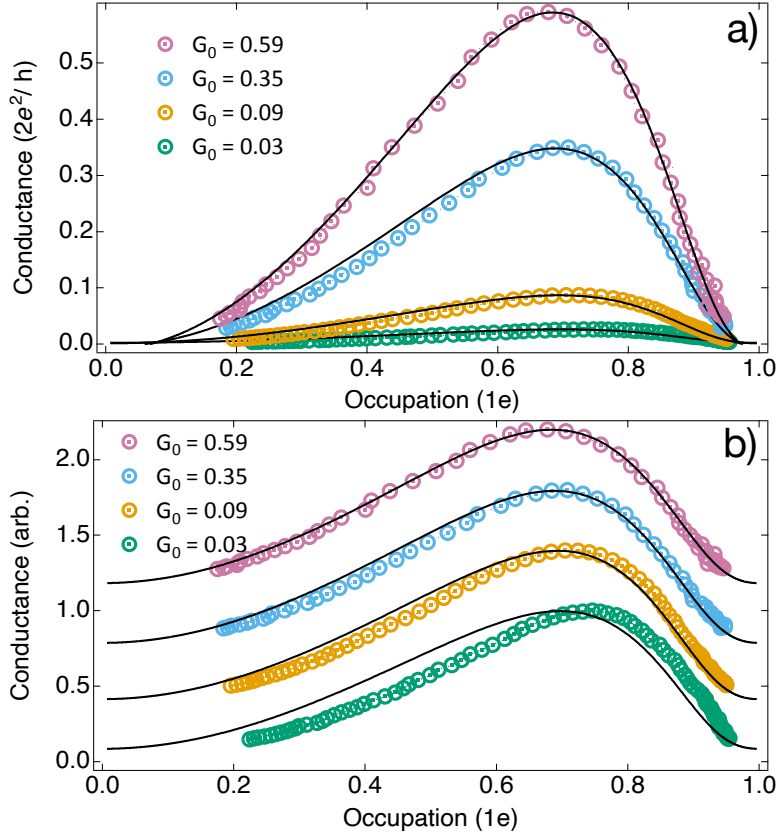


Figure 4.7: (a) Conductance versus occupation ($\Gamma/k_B T = 21$) with different ratios of coupling symmetry between the two leads of the dot. As the asymmetry is increased, the conductance decreases. (b) Same data as in (a), except the traces are offset and scaled for clarity. Symmetric coupling agrees well with NRG calculations. However, the asymmetrically coupled data is shifted to the right of the predicted NRG. This suggests that $\Gamma/k_B T$ extracted from the global fit to conductance is lower than expected.

temperature broadening, so the results cannot be extrapolated to our regime of zero bias.

An early study on the shape of the charge transition with symmetric coupling found that in the absence of a magnetic field, charge transitions are unaffected by the onset of Kondo correlations [72]. It was argued that

4.5. Kondo Effect with Varying Coupling Symmetry

the conductance enhancement between Coulomb peaks results from a larger number of electrons traversing the quantum dot, each dwelling there for a shorter time. However, coupling symmetry was not explored in this experiment.

An interesting insight comes from very recent theoretical studies of the differential conductance through a quantum dot and its dependence on asymmetry in the tunnel barriers and source-drain bias [73], [74]. It was found that higher-order corrections to the differential conductance include non-linear terms that depend strongly on the tunnelling and bias asymmetries. To qualitatively explain how this might occur, for $\Gamma_L > \Gamma_R$, the number of electrons entering the quantum dot from the left side becomes larger than the number of electrons leaving the right side. Therefore, the number of electrons in the dot increases and the repulsive interaction increases $\tilde{\epsilon}_0$. In contrast, $\tilde{\epsilon}_0$ would decrease for $\Gamma_L < \Gamma_R$. This modification to $\tilde{\epsilon}_0$ can result in increased or decreased conductance. However, corrections to the differential conductance require an applied bias across the quantum dot. Although $1\mu\text{V}$ bias is applied across the dot, we consider this effectively zero bias as it is much smaller than the thermal broadening.

It should be noted that the exploration of coupling symmetry in this thesis only came from two overnight measurements in a single cooldown and a second cooldown is required to verify the findings. Additionally, a subsequent cooldown would allow for a more focused exploration of tunnel coupling and bias symmetry.

Chapter 5

Conclusion

“Nothing in life is to be feared, it is only to be understood. Now is the time to understand more, so that we may fear less.”

MARIE CURIE

In conclusion, a method has been demonstrated to study the conductance enhancement from the Kondo effect, in a more weakly coupled regime than has been previously explored. Previous studies have predominantly focused on very strong coupling, where the Kondo temperature exceeds the system temperature, even between Coulomb peaks. Weaker coupling reveals a markedly different behaviour: the Kondo temperature is significantly lower than the system temperature between Coulomb peaks, resulting in a lack of conductance enhancement. Nonetheless, as the dot energy approaches the Fermi energy of the source and drain leads, the Kondo temperature increases exponentially. Consequently, even under relatively weak coupling, a small conductance enhancement persists on the shoulder of odd occupation Coulomb peaks.

To reliably measure this small conductance enhancement, a new method is required to disentangle the effects of charge motion, entropy, and Kondo enhancement on the shape and location of the conductance. The approach relies on two key components. The first component is a simultaneous measurement of a conductance and charge transition. The charge transition is then used to determine the occupation of the quantum dot. This occupation is used as a reference to remove the effects of charge motion and entropy. When conductance is plotted against the occupation, a shift in the maximum conduction to higher occupation suggests Kondo enhancement. The second component is measuring conductance at a range of temperatures that cross

Chapter 5. Conclusion

into the temperature broadened regime, $\Gamma/k_B T \lesssim 1$. A global fit to NRG, including each temperature setpoint is used to reliably determine $\Gamma/k_B T$ and lever arm. The determined $\Gamma/k_B T$ is then used to compare data with NRG to test agreement.

Agreement between data and corresponding NRG is seen at coupling strengths $\Gamma/k_B T = 20.5$, $\Gamma/k_B T = 9.7$ and $\Gamma/k_B T = 2.5$. The most strongly coupled data ($\Gamma/k_B T = 20.5$) shows the greatest shift in conductance maximum towards higher occupation. A reliable measurement of the charge transition is critical to determine the occupation of the quantum dot. Hence, various current setpoints through the charge sensor were tested to ensure independence from the charge sensor's settings. Despite differences in the underlying charge transition shape across current setpoints, agreement with NRG was consistently observed. To investigate the influence of coupling symmetry on Kondo enhancement, four ratios of coupling symmetry were measured. Good agreement with NRG was found with symmetric coupling. However, a shift towards greater occupation than predicted by NRG was observed as coupling symmetry became more asymmetric. This discrepancy suggests a difference between the $\Gamma/k_B T$ value determined from the global fits to conductance and that which best matches the corresponding charge transitions. To validate this observation, separate global fits to conductance and charge transitions were performed. Under symmetric coupling, the determined $\Gamma/k_B T$ values agree. However, as asymmetry increases, the $\Gamma/k_B T$ obtained from the charge transitions is significantly larger than that from the conductance fits. The discrepancy with NRG is surprising as conversations with our theorist collaborators suggest that NRG only depends on the overall Γ , and not the ratio between Γ_L and Γ_R .

To my knowledge, only one other experiment has investigated the effects of coupling symmetry on the Kondo effect [65]. It was found that the characteristic zero bias peak between Coulomb peaks shifted to a nonzero bias. However, this effect would require a strong energy dependence of the tunnel barriers (i.e., $\Gamma = \Gamma(E)$) in a NRG calculation, which is not assumed in our current NRG calculations.

An interesting insight into our observed discrepancy comes from very

Chapter 5. Conclusion

recent theoretical studies of the differential conductance through a quantum dot and its dependence on asymmetry in the tunnel barriers and source-drain bias [73], [74]. It was found that higher-order corrections to the differential conductance include non-linear terms that depend strongly on the tunnelling and bias asymmetries. However, corrections to the differential conductance in this paper require an applied bias across the quantum dot. As the measurements in this thesis were conducted in an effective zero bias limit ($1\text{ }\mu\text{V}$ bias), it is unclear whether the discrepancy can be explained by this theory. A further cooldown would allow for a more focused exploration of tunnel coupling symmetry, bias symmetry and total applied bias. If our data qualitatively matches these recent theory predictions, a new calculation of our NRG, including bias and tunnel coupling symmetry may be required.

Finally, a recent study observed the change in entropy as an electron entered a quantum dot (coupled to a single lead) with similar coupling strengths as those in this thesis [28]. A suppression of the entropy was reported, however, the expected shift in the entropy onset was not seen in the data. In contrast, the measurements on asymmetric coupling in this thesis found the conductance maximum shifts towards greater occupation than predicted by NRG. Perhaps a device capable of measuring entropy and conductance with two leads holds promise for illuminating this discrepancy.

Bibliography

- [1] R. El-Dardiry and R. Knuiman. “In interview with professor carlo beenakker.” natuurkunde.nl, Ed. (Feb. 2006), [Online]. Available: <https://www.natuurkunde.nl/artikelen/2877/carlo-beenakker>.
- [2] B. J. van Wees, H. van Houten, C. W. J. Beenakker, *et al.*, “Quantized conductance of point contacts in a two-dimensional electron gas,” *Physical Review Letters*, vol. 60, no. 9, pp. 848–850, Feb. 1988, ISSN: 0031-9007. DOI: [10.1103/physrevlett.60.848](https://doi.org/10.1103/physrevlett.60.848).
- [3] D. A. Wharam, T. J. Thornton, R. Newbury, *et al.*, “One-dimensional transport and the quantisation of the ballistic resistance,” *Journal of Physics C: Solid State Physics*, vol. 21, no. 8, pp. L209–L214, Mar. 1988, ISSN: 0022-3719. DOI: [10.1088/0022-3719/21/8/002](https://doi.org/10.1088/0022-3719/21/8/002).
- [4] U. Meirav, M. A. Kastner, and S. J. Wind, “Single-electron charging and periodic conductance resonances in GaAs nanostructures,” *Physical Review Letters*, vol. 65, no. 6, pp. 771–774, Aug. 1990, ISSN: 0031-9007. DOI: [10.1103/physrevlett.65.771](https://doi.org/10.1103/physrevlett.65.771).
- [5] S. Metti, C. Thomas, D. Xiao, and M. J. Manfra, “Spin-orbit coupling and electron scattering in high-quality $\text{InSb}_{1-x}\text{As}_x$ quantum wells,” *Physical Review B*, vol. 106, no. 16, Oct. 2022, ISSN: 2469-9969. DOI: [10.1103/physrevb.106.165304](https://doi.org/10.1103/physrevb.106.165304).
- [6] T. Child, O. Sheekey, S. Lüscher, *et al.*, “Entropy measurement of a strongly coupled quantum dot,” *Physical Review Letters*, vol. 129, no. 22, Nov. 2022, ISSN: 1079-7114. DOI: [10.1103/physrevlett.129.227702](https://doi.org/10.1103/physrevlett.129.227702).

BIBLIOGRAPHY

- [7] F. Borsoi, N. W. Hendrickx, V. John, *et al.*, “Shared control of a 16 semiconductor quantum dot crossbar array,” *Nature Nanotechnology*, vol. 19, no. 1, pp. 21–27, Aug. 2023, ISSN: 1748-3395. DOI: 10.1038/s41565-023-01491-3.
- [8] R. Su, M. Kuiri, K. Watanabe, T. Taniguchi, and J. Folk, “Superconductivity in twisted double bilayer graphene stabilized by WSe₂,” *Nature Materials*, vol. 22, no. 11, pp. 1332–1337, Aug. 2023, ISSN: 1476-4660. DOI: 10.1038/s41563-023-01653-7.
- [9] E. Y. Andrei, G. Deville, D. C. Glattli, F. I. B. Williams, E. Paris, and B. Etienne, “Observation of a magnetically induced wigner solid,” *Physical Review Letters*, vol. 60, no. 26, pp. 2765–2768, Jun. 1988, ISSN: 0031-9007. DOI: 10.1103/physrevlett.60.2765.
- [10] K. S. Novoselov, A. K. Geim, S. V. Morozov, *et al.*, “Electric field effect in atomically thin carbon films,” *Science*, vol. 306, no. 5696, pp. 666–669, Oct. 2004, ISSN: 1095-9203. DOI: 10.1126/science.1102896.
- [11] V. J. Goldman and B. Su, “Resonant tunneling in the quantum hall regime: Measurement of fractional charge,” *Science*, vol. 267, no. 5200, pp. 1010–1012, Feb. 1995, ISSN: 1095-9203. DOI: 10.1126/science.267.5200.1010.
- [12] K. v. Klitzing, G. Dorda, and M. Pepper, “New method for high-accuracy determination of the fine-structure constant based on quantized hall resistance,” *Physical Review Letters*, vol. 45, no. 6, pp. 494–497, Aug. 1980, ISSN: 0031-9007. DOI: 10.1103/physrevlett.45.494.
- [13] J. Barrier, P. Kumaravadivel, R. Krishna Kumar, *et al.*, “Long-range ballistic transport of brown-zak fermions in graphene superlattices,” *Nature Communications*, vol. 11, no. 1, Nov. 2020, ISSN: 2041-1723. DOI: 10.1038/s41467-020-19604-0.
- [14] W. de Haas, J. de Boer, and G. van den Berg, “The electrical resistance of gold, copper and lead at low temperatures,” *Physica*, vol. 1, no. 7–12, pp. 1115–1124, May 1934, ISSN: 0031-8914. DOI: 10.1016/s0031-8914(34)80310-2.

BIBLIOGRAPHY

- [15] J. Kondo, “Resistance minimum in dilute magnetic alloys,” *Progress of Theoretical Physics*, vol. 32, no. 1, pp. 37–49, Jul. 1964, ISSN: 1347-4081. DOI: [10.1143/ptp.32.37](https://doi.org/10.1143/ptp.32.37).
- [16] T. A. Costi, A. C. Hewson, and V. Zlatic, “Transport coefficients of the anderson model via the numerical renormalization group,” *Journal of Physics: Condensed Matter*, vol. 6, no. 13, pp. 2519–2558, Mar. 1994, ISSN: 1361-648X. DOI: [10.1088/0953-8984/6/13/013](https://doi.org/10.1088/0953-8984/6/13/013).
- [17] W. G. van der Wiel, S. D. Franceschi, T. Fujisawa, J. M. Elzerman, S. Tarucha, and L. P. Kouwenhoven, “The kondo effect in the unitary limit,” *Science*, vol. 289, no. 5487, pp. 2105–2108, Sep. 2000, ISSN: 1095-9203. DOI: [10.1126/science.289.5487.2105](https://doi.org/10.1126/science.289.5487.2105).
- [18] A. Kawabata, “On the electron transport through a quantum dot,” *Journal of the Physical Society of Japan*, vol. 60, no. 10, pp. 3222–3225, Oct. 1991, ISSN: 1347-4073. DOI: [10.1143/jpsj.60.3222](https://doi.org/10.1143/jpsj.60.3222).
- [19] Y. Meir, N. S. Wingreen, and P. A. Lee, “Low-temperature transport through a quantum dot: The anderson model out of equilibrium,” *Physical Review Letters*, vol. 70, no. 17, pp. 2601–2604, Apr. 1993, ISSN: 0031-9007. DOI: [10.1103/physrevlett.70.2601](https://doi.org/10.1103/physrevlett.70.2601).
- [20] C. Tong, A. Kurzmann, R. Garreis, *et al.*, “Pauli blockade catalogue and three- and four-particle kondo effect in bilayer graphene quantum dots,” *Physical Review Research*, vol. 6, no. 1, Jan. 2024, ISSN: 2643-1564. DOI: [10.1103/physrevresearch.6.1012006](https://doi.org/10.1103/physrevresearch.6.1012006).
- [21] S. Seiro, L. Jiao, S. Kirchner, *et al.*, “Evolution of the kondo lattice and non-fermi liquid excitations in a heavy-fermion metal,” *Nature Communications*, vol. 9, no. 1, Aug. 2018, ISSN: 2041-1723. DOI: [10.1038/s41467-018-05801-5](https://doi.org/10.1038/s41467-018-05801-5).
- [22] R. M. Potok, I. G. Rau, H. Shtrikman, Y. Oreg, and D. Goldhaber-Gordon, “Observation of the two-channel kondo effect,” *Nature*, vol. 446, no. 7132, pp. 167–171, Mar. 2007, ISSN: 1476-4687. DOI: [10.1038/nature05556](https://doi.org/10.1038/nature05556).

BIBLIOGRAPHY

- [23] Z. Iftikhar, S. Jezouin, A. Anthore, *et al.*, “Two-channel kondo effect and renormalization flow with macroscopic quantum charge states,” *Nature*, vol. 526, no. 7572, pp. 233–236, Oct. 2015, ISSN: 1476-4687. DOI: [10.1038/nature15384](https://doi.org/10.1038/nature15384).
- [24] S. Kirchner, “Two-channel kondo physics: From engineered structures to quantum materials realizations,” *Advanced Quantum Technologies*, vol. 3, no. 5, Mar. 2020, ISSN: 2511-9044. DOI: [10.1002/qute.201900128](https://doi.org/10.1002/qute.201900128).
- [25] B. Béri and N. R. Cooper, “Topological kondo effect with majorana fermions,” *Physical Review Letters*, vol. 109, no. 15, Oct. 2012, ISSN: 1079-7114. DOI: [10.1103/physrevlett.109.156803](https://doi.org/10.1103/physrevlett.109.156803).
- [26] G. Li, Y. Oreg, and J. I. Väyrynen, “Multichannel topological kondo effect,” *Physical Review Letters*, vol. 130, no. 6, Feb. 2023, ISSN: 1079-7114. DOI: [10.1103/physrevlett.130.066302](https://doi.org/10.1103/physrevlett.130.066302).
- [27] S. Bollmann, J. I. Väyrynen, and E. J. König, “Topological kondo effect with spinful majorana fermions,” 2024. DOI: [10.48550/ARXIV.2402.05931](https://arxiv.org/abs/2402.05931).
- [28] T. Child, O. Sheekey, S. Lüscher, *et al.*, “Entropy measurement of a strongly coupled quantum dot,” *Physical Review Letters*, vol. 129, no. 22, Nov. 2022, ISSN: 1079-7114. DOI: [10.1103/physrevlett.129.227702](https://doi.org/10.1103/physrevlett.129.227702).
- [29] I. Newton, *The Correspondence of Isaac Newton: Volume I 1661–1675*, H. W. Turnbull, Ed. Cambridge University Press, Jan. 1959, ISBN: 9780521737838. DOI: [10.1017/9781108699945](https://doi.org/10.1017/9781108699945).
- [30] M. J. Manfra, “Molecular beam epitaxy of ultra-high-quality AlGaAs/GaAs heterostructures: Enabling physics in low-dimensional electronic systems,” *Annual Review of Condensed Matter Physics*, vol. 5, no. 1, pp. 347–373, Mar. 2014, ISSN: 1947-5462. DOI: [10.1146/annurev-conmatphys-031113-133905](https://doi.org/10.1146/annurev-conmatphys-031113-133905).

BIBLIOGRAPHY

- [31] S. Adachi, *GaAs and Related Materials: Bulk Semiconducting and Superlattice Properties*. WORLD SCIENTIFIC, Oct. 1994, ISBN: 9789812705709. DOI: [10.1142/2508](https://doi.org/10.1142/2508).
- [32] R. Dingle, H. L. Störmer, A. C. Gossard, and W. Wiegmann, “Electron mobilities in modulation-doped semiconductor heterojunction superlattices,” *Applied Physics Letters*, vol. 33, no. 7, pp. 665–667, Oct. 1978, ISSN: 1077-3118. DOI: [10.1063/1.90457](https://doi.org/10.1063/1.90457).
- [33] C. Beenakker and H. van Houten, “Quantum transport in semiconductor nanostructures,” in *Solid State Physics*. Elsevier, 1991, pp. 1–228. DOI: [10.1016/s0081-1947\(08\)60091-0](https://doi.org/10.1016/s0081-1947(08)60091-0).
- [34] L. L. Chang, L. Esaki, W. E. Howard, and R. Ludeke, “The growth of a GaAs – GaAlAs superlattice,” *Journal of Vacuum Science and Technology*, vol. 10, no. 1, pp. 11–16, Jan. 1973, ISSN: 0022-5355. DOI: [10.1116/1.1317919](https://doi.org/10.1116/1.1317919).
- [35] D. Waddington, A. Burke, S. Fricke, *et al.*, “Can insulating the gates lead us to stable modulation-doped hole quantum devices?” In *2010 Conference on Optoelectronic and Microelectronic Materials and Devices*, IEEE, Dec. 2010. DOI: [10.1109/commad.2010.5699738](https://doi.org/10.1109/commad.2010.5699738).
- [36] J. H. Davies, I. A. Larkin, and E. V. Sukhorukov, “Modeling the patterned two-dimensional electron gas: Electrostatics,” *Journal of Applied Physics*, vol. 77, no. 9, pp. 4504–4512, May 1995, ISSN: 1089-7550. DOI: [10.1063/1.359446](https://doi.org/10.1063/1.359446).
- [37] M. Field, C. G. Smith, M. Pepper, *et al.*, “Measurements of coulomb blockade with a noninvasive voltage probe,” *Physical Review Letters*, vol. 70, no. 9, pp. 1311–1314, Mar. 1993, ISSN: 0031-9007. DOI: [10.1103/physrevlett.70.1311](https://doi.org/10.1103/physrevlett.70.1311).
- [38] R. Hanson, L. P. Kouwenhoven, J. R. Petta, S. Tarucha, and L. M. K. Vandersypen, “Spins in few-electron quantum dots,” *Reviews of Modern Physics*, vol. 79, no. 4, pp. 1217–1265, Oct. 2007, ISSN: 1539-0756. DOI: [10.1103/revmodphys.79.1217](https://doi.org/10.1103/revmodphys.79.1217).

BIBLIOGRAPHY

- [39] I. Giaever and H. R. Zeller, “Superconductivity of small tin particles measured by tunneling,” *Physical Review Letters*, vol. 20, no. 26, pp. 1504–1507, Jun. 1968, ISSN: 0031-9007. DOI: [10.1103/physrevlett.20.1504](https://doi.org/10.1103/physrevlett.20.1504).
- [40] L. P. Kouwenhoven, C. M. Marcus, P. L. McEuen, S. Tarucha, R. M. Westervelt, and N. S. Wingreen, “Electron transport in quantum dots,” in *Mesoscopic Electron Transport*. Springer Netherlands, 1997, pp. 105–214, ISBN: 9789401588393. DOI: [10.1007/978-94-015-8839-3_4](https://doi.org/10.1007/978-94-015-8839-3_4).
- [41] C. W. J. Beenakker, “Theory of coulomb-blockade oscillations in the conductance of a quantum dot,” *Physical Review B*, vol. 44, no. 4, pp. 1646–1656, Jul. 1991, ISSN: 1095-3795. DOI: [10.1103/physrevb.44.1646](https://doi.org/10.1103/physrevb.44.1646).
- [42] M. Field, C. G. Smith, M. Pepper, *et al.*, “Measurements of coulomb blockade with a noninvasive voltage probe,” *Physical Review Letters*, vol. 70, no. 9, pp. 1311–1314, Mar. 1993, ISSN: 0031-9007. DOI: [10.1103/physrevlett.70.1311](https://doi.org/10.1103/physrevlett.70.1311).
- [43] R. Schleser, E. Ruh, T. Ihn, K. Ensslin, D. C. Driscoll, and A. C. Gossard, “Time-resolved detection of individual electrons in a quantum dot,” *Applied Physics Letters*, vol. 85, no. 11, pp. 2005–2007, Sep. 2004, ISSN: 1077-3118. DOI: [10.1063/1.1784875](https://doi.org/10.1063/1.1784875).
- [44] L. M. K. Vandersypen, J. M. Elzerman, R. N. Schouten, L. H. Willems van Beveren, R. Hanson, and L. P. Kouwenhoven, “Real-time detection of single-electron tunneling using a quantum point contact,” *Applied Physics Letters*, vol. 85, no. 19, pp. 4394–4396, Nov. 2004, ISSN: 1077-3118. DOI: [10.1063/1.1815041](https://doi.org/10.1063/1.1815041).
- [45] L.-X. Zhang, J. P. Leburton, R. Hanson, and L. P. Kouwenhoven, “Engineering the quantum point contact response to single-electron charging in a few-electron quantum-dot circuit,” *Applied Physics Letters*, vol. 85, no. 13, pp. 2628–2630, Sep. 2004, ISSN: 1077-3118. DOI: [10.1063/1.1790605](https://doi.org/10.1063/1.1790605).

BIBLIOGRAPHY

- [46] S. Gustavsson, R. Leturcq, M. Studer, *et al.*, “Electron counting in quantum dots,” *Surface Science Reports*, vol. 64, no. 6, pp. 191–232, Jun. 2009, ISSN: 0167-5729. DOI: [10.1016/j.surfrept.2009.02.001](https://doi.org/10.1016/j.surfrept.2009.02.001).
- [47] M. de Kruijf, G. M. Noah, A. Gomez-Saiz, J. J. L. Morton, and M. F. Gonzalez-Zalba, “Measurement of cryoelectronics heating using a local quantum dot thermometer in silicon,” 2023. DOI: [10.48550/ARXIV.2310.11383](https://arxiv.org/abs/2310.11383).
- [48] S. Liang, J. Nakamura, G. C. Gardner, and M. J. Manfra, “Reduction of charge noise in shallow GaAs/AlGaAs heterostructures with insulated gates,” *Applied Physics Letters*, vol. 117, no. 13, Sep. 2020, ISSN: 1077-3118. DOI: [10.1063/5.0026259](https://doi.org/10.1063/5.0026259).
- [49] C. Buizert, F. H. L. Koppens, M. Pioro-Ladrière, *et al.*, “*InSitu* Reduction of charge noise in GaAs/Al_xGa_{1-x}As schottky-gated devices,” *Physical Review Letters*, vol. 101, no. 22, Nov. 2008, ISSN: 1079-7114. DOI: [10.1103/physrevlett.101.226603](https://doi.org/10.1103/physrevlett.101.226603).
- [50] D. Goldhaber-Gordon, H. Shtrikman, D. Mahalu, D. Abusch-Magder, U. Meirav, and M. A. Kastner, “Kondo effect in a single-electron transistor,” *Nature*, vol. 391, no. 6663, pp. 156–159, Jan. 1998, ISSN: 1476-4687. DOI: [10.1038/34373](https://doi.org/10.1038/34373).
- [51] Unknown, “Still irresistible,” *Nature Physics*, vol. 10, no. 5, pp. 329–329, Apr. 2014, ISSN: 1745-2481. DOI: [10.1038/nphys2972](https://doi.org/10.1038/nphys2972).
- [52] A. C. Hewson, *The Kondo Problem to Heavy Fermions*. Cambridge University Press, Jan. 1993, ISBN: 9780511470752. DOI: [10.1017/cbo9780511470752](https://doi.org/10.1017/cbo9780511470752).
- [53] G. D. Mahan, *Many-Particle Physics*. Springer US, 2000, ISBN: 9781475757149. DOI: [10.1007/978-1-4757-5714-9](https://doi.org/10.1007/978-1-4757-5714-9).
- [54] T. Yanagisawa, “From resistance minimum to kondo physics,” *New Physics: Sae Mulli*, vol. 73, no. 12, pp. 1098–1109, Dec. 2023, ISSN: 2289-0041. DOI: [10.3938/npsm.73.1098](https://doi.org/10.3938/npsm.73.1098).

BIBLIOGRAPHY

- [55] H. C. Manoharan, C. P. Lutz, and D. M. Eigler, “Quantum mirages formed by coherent projection of electronic structure,” *Nature*, vol. 403, no. 6769, pp. 512–515, Feb. 2000, ISSN: 1476-4687. DOI: 10.1038/35000508.
- [56] F. D. M. Haldane, “Scaling theory of the asymmetric anderson model,” *Physical Review Letters*, vol. 40, no. 6, pp. 416–419, Feb. 1978, ISSN: 0031-9007. DOI: 10.1103/physrevlett.40.416.
- [57] J. D. Schmid, *The kondo effect in quantum dots*, en, 2000. DOI: 10.18419/OPUS-6476.
- [58] D. Goldhaber-Gordon, J. Göres, M. A. Kastner, H. Shtrikman, D. Mahalu, and U. Meirav, “From the kondo regime to the mixed-valence regime in a single-electron transistor,” *Physical Review Letters*, vol. 81, no. 23, pp. 5225–5228, Dec. 1998, ISSN: 1079-7114. DOI: 10.1103/physrevlett.81.5225.
- [59] M. Pustilnik and L. Glazman, “Kondo effect in quantum dots,” *Journal of Physics: Condensed Matter*, vol. 16, no. 16, R513–R537, Apr. 2004, ISSN: 1361-648X. DOI: 10.1088/0953-8984/16/16/r01.
- [60] S. M. Cronenwett, T. H. Oosterkamp, and L. P. Kouwenhoven, “A tunable kondo effect in quantum dots,” *Science*, vol. 281, no. 5376, pp. 540–544, Jul. 1998, ISSN: 1095-9203. DOI: 10.1126/science.281.5376.540.
- [61] N. Hartman, C. Olsen, S. Lüscher, *et al.*, “Direct entropy measurement in a mesoscopic quantum system,” *Nature Physics*, vol. 14, no. 11, pp. 1083–1086, Aug. 2018, ISSN: 1745-2481. DOI: 10.1038/s41567-018-0250-5.
- [62] M. Avinun-Kalish, M. Heiblum, A. Silva, D. Mahalu, and V. Umansky, “Controlled dephasing of a quantum dot in the kondo regime,” *Physical Review Letters*, vol. 92, no. 15, Apr. 2004, ISSN: 1079-7114. DOI: 10.1103/physrevlett.92.156801.

BIBLIOGRAPHY

- [63] G. Breit and E. Wigner, “Capture of slow neutrons,” *Physical Review*, vol. 49, no. 7, pp. 519–531, Apr. 1936, ISSN: 0031-899X. DOI: [10.1103/physrev.49.519](https://doi.org/10.1103/physrev.49.519).
- [64] K. G. Wilson, “The renormalization group: Critical phenomena and the kondo problem,” *Reviews of Modern Physics*, vol. 47, no. 4, pp. 773–840, Oct. 1975, ISSN: 0034-6861. DOI: [10.1103/revmodphys.47.773](https://doi.org/10.1103/revmodphys.47.773).
- [65] F. Simmel, R. H. Blick, J. P. Kotthaus, W. Wegscheider, and M. Bichler, “Anomalous kondo effect in a quantum dot at nonzero bias,” *Physical Review Letters*, vol. 83, no. 4, pp. 804–807, Jul. 1999, ISSN: 1079-7114. DOI: [10.1103/physrevlett.83.804](https://doi.org/10.1103/physrevlett.83.804).
- [66] A. Silva and S. Levit, “Peculiarities of the controlled dephasing of a quantum dot in the kondo regime,” *Europhysics Letters (EPL)*, vol. 62, no. 1, pp. 103–109, Apr. 2003, ISSN: 1286-4854. DOI: [10.1209/epl/i2003-00368-1](https://doi.org/10.1209/epl/i2003-00368-1).
- [67] K. MacLean, S. Amasha, I. P. Radu, *et al.*, “Energy-dependent tunneling in a quantum dot,” *Physical Review Letters*, vol. 98, no. 3, Jan. 2007, ISSN: 1079-7114. DOI: [10.1103/physrevlett.98.036802](https://doi.org/10.1103/physrevlett.98.036802).
- [68] T. Ihn, S. Gustavsson, U. Gasser, *et al.*, “Quantum dots investigated with charge detection techniques,” *Solid State Communications*, vol. 149, no. 35–36, pp. 1419–1426, Sep. 2009, ISSN: 0038-1098. DOI: [10.1016/j.ssc.2009.04.040](https://doi.org/10.1016/j.ssc.2009.04.040).
- [69] B. Küng, C. Rössler, M. Beck, J. Faist, T. Ihn, and K. Ensslin, “Quantum dot occupation and electron dwell time in the cotunneling regime,” *New Journal of Physics*, vol. 14, no. 8, p. 083 003, Aug. 2012, ISSN: 1367-2630. DOI: [10.1088/1367-2630/14/8/083003](https://doi.org/10.1088/1367-2630/14/8/083003).
- [70] M. C. Rogge, B. Harke, C. Fricke, *et al.*, “Coupling symmetry of quantum dot states,” *Physical Review B*, vol. 72, no. 23, Dec. 2005, ISSN: 1550-235X. DOI: [10.1103/physrevb.72.233402](https://doi.org/10.1103/physrevb.72.233402).
- [71] S. Gustavsson, R. Leturcq, B. Simović, *et al.*, “Counting statistics of single electron transport in a quantum dot,” *Physical Review Letters*,

vol. 96, no. 7, Feb. 2006, ISSN: 1079-7114. DOI: 10.1103/physrevlett.96.076605.

- [72] D. Sprinzak, Y. Ji, M. Heiblum, D. Mahalu, and H. Shtrikman, “Charge distribution in a kondo-correlated quantum dot,” *Physical Review Letters*, vol. 88, no. 17, Apr. 2002, ISSN: 1079-7114. DOI: 10.1103/physrevlett.88.176805.
- [73] K. Tsutsumi, Y. Teratani, R. Sakano, and A. Oguri, “Nonlinear fermi liquid transport through a quantum dot in asymmetric tunnel junctions,” *Physical Review B*, vol. 104, no. 23, Dec. 2021, ISSN: 2469-9969. DOI: 10.1103/physrevb.104.235147.
- [74] K. Tsutsumi, Y. Teratani, K. Motoyama, R. Sakano, and A. Oguri, “Role of bias and tunneling asymmetries in nonlinear fermi-liquid transport through an SU(N) quantum dot,” *Physical Review B*, vol. 108, no. 4, Jul. 2023, ISSN: 2469-9969. DOI: 10.1103/physrevb.108.045109.
- [75] C. W. Groth, M. Wimmer, A. R. Akhmerov, and X. Waintal, “Kwant: A software package for quantum transport,” *New Journal of Physics*, vol. 16, no. 6, p. 063065, Jun. 2014, ISSN: 1367-2630. DOI: 10.1088/1367-2630/16/6/063065.

Appendix A

Quantum Device Fabrication

During my Master's studies, I was trained by Timothy Child on the necessary fabrication steps to add inner and outer gates forming the quantum devices. Once fully qualified, I fabricated some devices on my own. There are a number of required steps to turn the GaAs/AlGaAs heterostructures received from Michael Manfra's group into a chip that we can then add the inner and outer gates. It should also be noted that I made no contribution to the nano fabrication recipes and simply followed the procedure developed by previous students. The following summary is largely adapted from Owen Sheekey's thesis, a past student from the Quantum Devices Group.

A.1 Summary

The GaAs substrates are grown by Michael Manfra's group at Purdue University. There are two key features to devices built on GaAs/AlGaAs 2DEGs – ohmic contact to the 2DEG and gating structures. In overview, devices used for this project use a thin film of Al_2O_3 to electrically isolate top gates fabricated from Au/Ti. Ohmic contacts are made using annealed Ni/Au/Ge.

The general process of preparation of a sample goes as follows:

1. Gallium removal from back of wafers.
2. Ohmic contact: Lithography, evaporation, annealing.
3. Mesa etching: Lithography, H_2SO_4 etching.
4. Atomic layer deposition: Al_2O_3 .
5. Gating (2 steps): Lithography, evaporation.

A.2. Recipes

6. Wire bonding

A.2 Recipes

A.2.1 Gallium Removal

This is a recipe developed by Dr. Silvia Lüscher Folk.

1. Cleave a full wafer into a quarter or half wafer. Blow off any dust bunnies from the surface before starting.
2. Spin a layer of AZ1518 resists at 4000 RPM for 40 s.
3. Bake the resist for 2 minutes at 100°C.
4. Put a clean wipe on a hotplate and set to 50°C. Put wafer face down (gallium side up) onto the clean wipe.
5. Wipe off gallium with q tips. Keep wiping until it is all gone.
6. Spin and bake another layer of AZ1518 (4000 RPM 40 s and bake 100°C 2 minutes).
7. Etch 2 minutes in full strength HCl. Quench etch by transferring to DI water.
8. Rinse well in DI water. Blow dry.
9. Squirt down with Acetone to strip resist from the surface and immediately rinse with IPA.
10. Soak 3 minutes each in Toluene, Acetone, and IPA. Rinse with IPA and blow dry between each solvent. Spray down with DI water and blow dry.

A.2. Recipes

A.2.2 Mesa Etch

1. Solvent clean – Acetone, IPA. Rinse in DI, blow dry with N₂.
2. Prebake chip for 60 s at 110°C.
3. AZ5214-E in positive mode, ramp up 500 RPM for 2 s, spin at 4444 RPM for 40 s with 60 s softbake at 100°C.
4. Photo lithography in MLA150 Heidelberg (Maskless Aligner) : Expose 90 mJ/cm², defocus -1
5. Develop in MIF 300, 50 s stop develop in DI.
6. Hardbake for 60 s at 120°C.
7. O₂ plasma etch in Plasma etch PE 50, 60s.
8. Etch in 30 mL diluted Sulfuric acid (700 Water:3 H₂S0₄) + 2 mL H₂O₂ at 18°C for 50 s
9. Stop etch in DI water. Remaining resist can be removed with Acetone, IPA and DI.

A.2.3 Ohmic Contact

Lithography and Evaporation

At the end of my Master's studies, there was a sizeable effort (that I was not involved in) to develop low resistance ohmic contacts by Vahid Mohaved and Dr. Silvia Lüscher Folk. Here is the most up to date recipe.

1. Solvent clean – Acetone, IPA, Ultrasound. Rinse in DI, blow dry with N₂.
2. Dehydration bake chip for 1 minutes at 110°C.
3. AZ5214-E in image reversal mode, ramp up 500 RPM for 2 s, spin at 4444 RPM for 50 s with 60 s softbake at 90°C.

A.2. Recipes

4. Photo lithography in MLA150 Heidelberg (Maskless Aligner) : Expose 40 mJ/cm², defocus +1
5. IR bake for 30 s at 110°C.
6. Photo lithography in MLA150 Heidelberg : Flood exposure 222 mJ/cm², defocus +1
7. Develop in AZ300 MIF , 40 s stop develop in DI.
8. Hardbake for 60 s at 110°C.
9. O² plasma etch in Plasma etch PE 50, 15 s.
10. Dip in 37% HCl for 20 s. Rinse with DI for 120 s
11. Evaporate the following:

Metal	Thickness	Rate
Ni	7 nm	1.0 Ås ⁻¹
Ge	80 nm	1.3 Ås ⁻¹
Au	160 nm	2.0 Ås ⁻¹
Ni	36 nm	1.6 Ås ⁻¹
Au	80 nm	1.7 Ås ⁻¹

12. Liftoff in Acetone at 70°C.
13. Rinse in Acetone, IPA and blowdry with N₂.

Annealing

The following process was followed on the rapid thermal annealer made “in house” for annealing GaAs and other substrates. The basic idea is to use a bulb in a near vacuum (with some amount of forming gas – H₂ + N₂) to heat the sample to a high temperature for a limited amount of time. The metal film melts and diffuses through the GaAs substrate to make contact with the 2DEG, usually 30 – 200 nm below the surface.

1. Pump down should reach lower limit, 0.133 mbar.

A.2. Recipes

2. Set regulator to 2.5 psi (forming gas).
3. Open Swagelock valve until pressure reads 10 mbar.
4. Close speedivalve until pressure reads 200 mbar.
5. Turn on bulb to roughly 34 %, it takes about 5 – 10 minutes
6. Wait at 350°C for 2 minutes
7. Go to 450°C as fast as you can, hold it there for 40 s.
8. Cool below 300°C fast by opening the speedivalve on the pump line all the way, and opening the gas flow.
9. Cool to 50°C, then vent and let cool to room temperature.

A.2.4 Gating

Gating is the process of adding metal to the top of the GaAs/AlGaAs heterostructure, which are then used to form and control the potential landscape in the 2DEG below (Fig. A.1). The overall recipe for gating was not varied during my fabrication time. However, if long periods have passed between fabrication (a few months), it is necessary to test an array of exposure doses for the E beam step as this parameter can vary over long periods of time and system re starts.

Inner Gates

1. Solvent clean - Acetone, IPA. Rinse in DI, blow dry with N₂.
2. Prebake chip for 3 minutes at 180°C.
3. Spin PMMA A2 495K at 5555 RPM for 50 s with 3 minutes bake at 180°C
4. Spin PMMA A1 950K at 3333 RPM for 50 s with 5 minutes bake at 180°C

A.2. Recipes

5. E beam lithography in Jeol JBX 8100FS : Dose 900 $\mu\text{C}/\text{cm}^2$
6. Develop in IPA:DI, 7:3 40 s at 18°C, stop by directly drying with N_2 .
7. Evaporate Ti 3 nm, 1.5 \AA s^{-1} then Au 12 nm 4 \AA s^{-1} .
8. Liftoff in Acetone at room temperature.

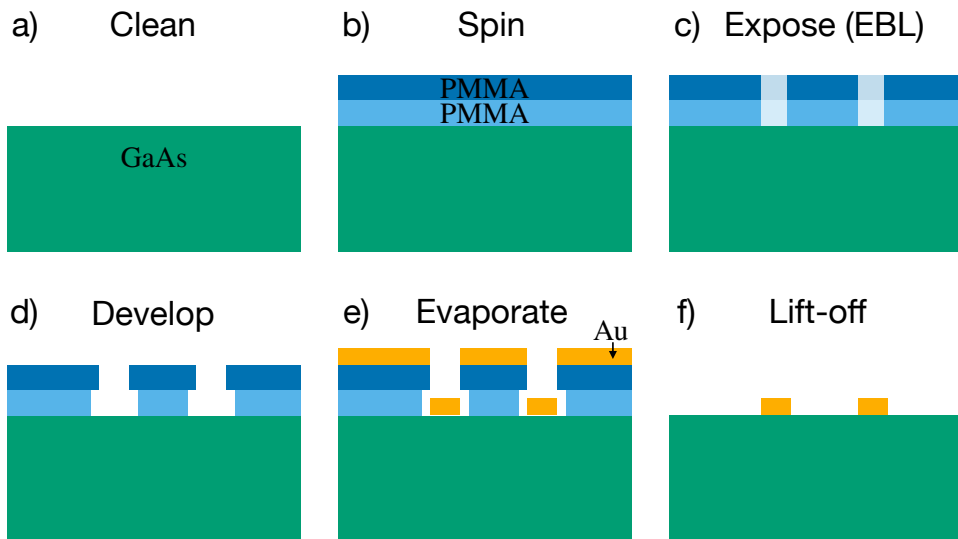


Figure A.1: (a) GaAs/AlGaAs heterostructure is cleaned in an Ultra Sonic (US) bath with acetone/IPA/DI. (b) Two different layers of PMMA are spun ontop of the heterostructure. (c) The gate design is exposed to an electron beam to breakup the PMMA. (d) The chip is developed in an IPA:DI solution create an undercut and remove the exposed PMMA. (e) 2:12 nm of Ti:Au are evaporated ontop of the chip. (f) The chip is rinsed in acetone to remove remaining PMMA and any metal attached to it. The chip is ready to be placed onto a chip carrier, wirebonded and measured.

Outer Gates and Bondpads

1. Solvent clean – Acetone, IPA. Rinse in DI, blow dry with N_2 .
2. Prebake chip for 3 minutes at 180°C.

A.2. Recipes

3. Spin PMMA A8 495K at 4000 RPM for 40 s with 3 minutes bake at 180°C
4. Spin PMMA A4 490K at 4000 RPM for 40 s with 5 minutes bake at 180°C
5. E beam lithography in Jeol JBX 8100FS : Dose 1100 $\mu\text{C}/\text{cm}^2$
6. Develop in IPA:DI, 7:3 40 s at 18°C, stop in DI.
7. O₂ plasma etch in Plasma etch PE 50, 1 minutes.
8. Evaporate Ti 10 nm, 2 \AA s^{-1} then Au 100 nm, 4 \AA s^{-1} .
9. Liftoff in Acetone at room temperature.

A.2.5 Wire Bonding

The final step in the fabrication process is to attach the chip to a chip carrier and connect the gates and ohmic contacts to bond pads (Fig. A.2). The chip carrier is added to the fridge and connected to the fridge wiring, which leads to a break-out box outside the fridge.

1. Stick the chip to the chip carrier using a small dab of PMMA A8 495K.
Bake for 5 minutes at 60°C
2. Wirebond bond pads on chip carrier to gates and ohmic contacts on the chip:

	Bond 1	Bond 2
Wire material	Al	Al
Bond strength	260	300
Bond duration	30 ms	30 ms

A.2. Recipes

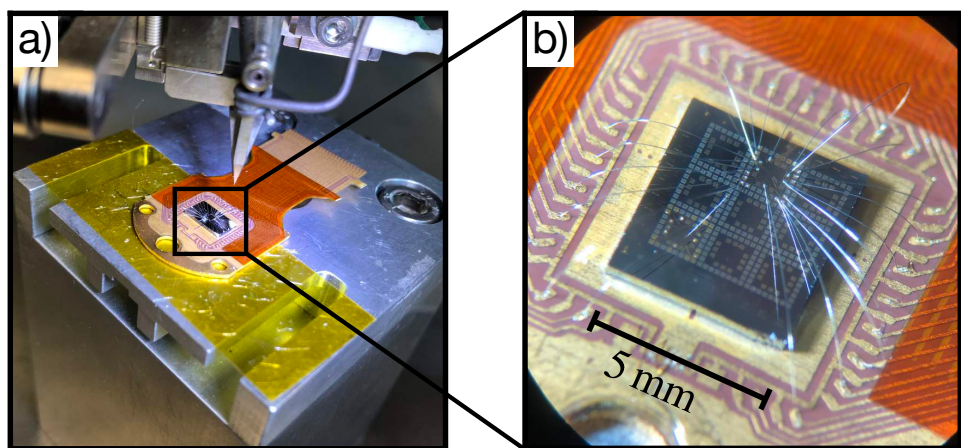


Figure A.2: (a) Chip carrier stuck to a platform under the wirebonder. (b) Close-up of the Al wire bonds that connect the device gates to a chip carrier.

Appendix B

Software

B.1 Open-Source Thesis

All L^AT_EX files, data and code used to build the figures in this thesis are available on GitHub.

The code can be found here:

https://github.com/johann997/QDEV_masters_thesis.

B.2 Data Acquisition and Analysis

I was fortunate to join FolkLab after Timothy Child had largely rewritten and significantly improved the acquisition code. However, code is never in a final state, and over the years, I contributed to the repository with new scan functions, analysis, and function dependency visualisation.

The code can be found here:

<https://github.com/folk-lab/IgorAcq>

For analysis, I built upon some initial code provided by Josh and Silvia. Currently, the code used to fit data to NRG lives in a separate repository from the acquisition code.

The code can be found here:

<https://github.com/johann997/KondoConductanceAnalysis>

B.3 Device Simulation

The code can be found here:

https://github.com/johann997/2deg_yodels

B.3. Device Simulation

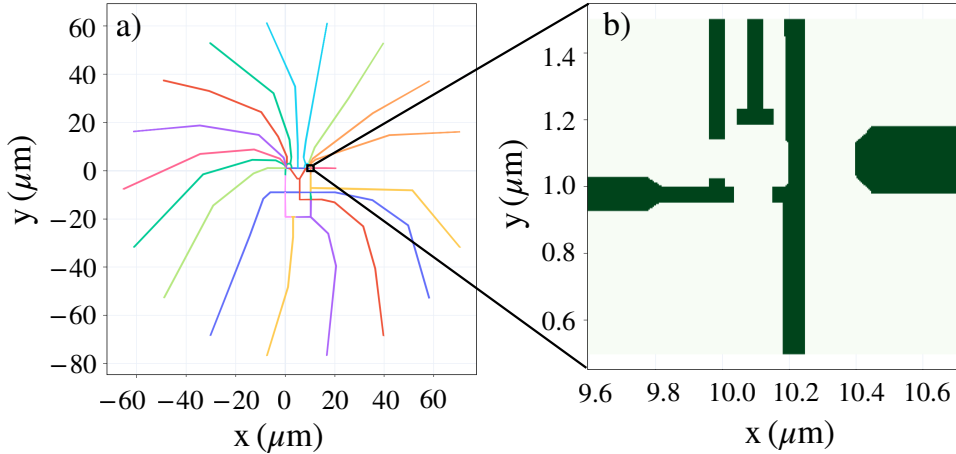


Figure B.1: **(a)** Plot of the uploaded .dxf. Each polyline in the .dxf is saved as a new trace (hence, the varying colours). **(b)** Discretised matrix from a zoom in on the uploaded design file. The matrix was defined by specifying the min, max and x, y coordinates and the number of points to discretise in the x and y direction (here numptsy and numptsy = 250). This approach is quite rudimentary and not optimised, but is sufficient at capturing the device design geometry.

Fabrication and measurement of quantum devices can be costly and time-consuming. As part of a class project, I developed an easy-to-install, open-source application that allows users to upload a .dxf file and calculate the electric potential from user-determined gate voltages. KWANT [75] is used to calculate transport properties by applying a tight-binding approximation. A tight-binding model reduces computation so that users can simulate pinch-off or charge stability diagrams in ‘real time’. This app aids the design process by providing quick, semi-quantitative information on design choices.

For user convenience, drag-and-drop functionality is used. Upon uploading the .dxf file, EZDXF Python library is used to extract the polylines. Users specify device areas by defining min, max and x, y coordinates, and point discretisation (Fig. B.1).

The electric potential is calculated using the method developed by Davies [36]. This method offers the advantage of computational efficiency.

B.3. Device Simulation

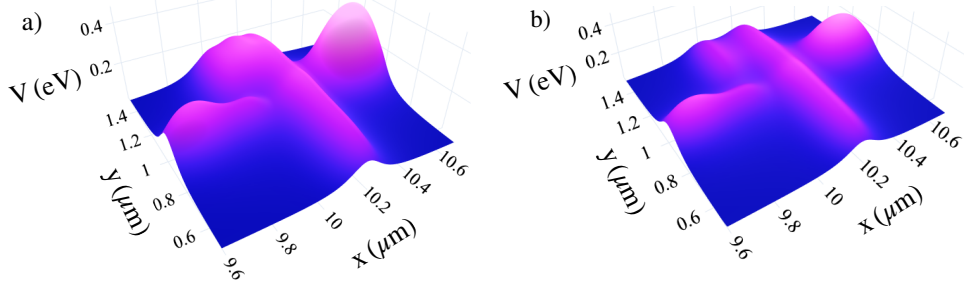


Figure B.2: (a) 3d map of the electrostatic potential landscape 90 nm below the surface of the heterostructure, calculated using the bare potentials on the gates on top of the heterostructure. (b) Varied potential landscape by changing the voltages on the gates.

A single ‘geometric factor’ is initially calculated and the resulting potential is simply the product of the geometric factor with the gate voltages. Real-time updates of the plotted potential are achieved using sliders (Fig. B.2). The disadvantage of this method is that screening terms are not included, and hence, the calculation can only be used as a qualitative visualisation of the electric potential profile.

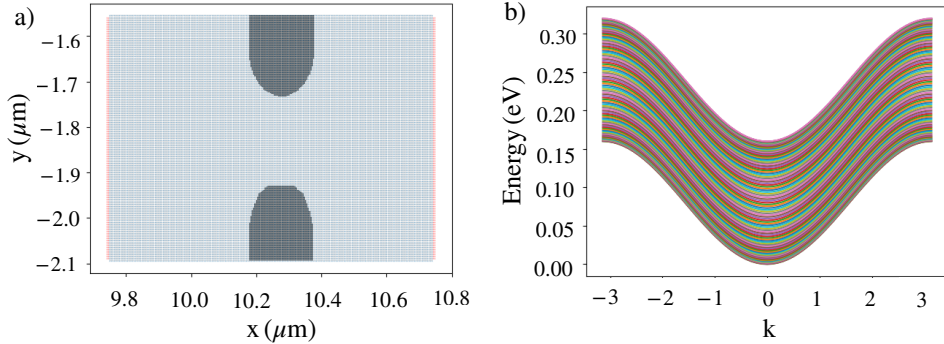


Figure B.3: (a) Gate design of a QPC on top of the KWANT [75], tight binding system. A square lattice with lattice constant 5 nm is chosen. The infinite leads are shown in red on the left and right axes. (b) Band structure calculation of this tight binding system. The user can calculate transport properties at the different allowed energy levels in the band structure.

B.3. Device Simulation

KWANT is utilised to build a tight-binding model which can be solved to provide access to transport properties [75]. This method assumes electrons are tightly bound to their respective atoms, with interactions from neighbouring atoms considered as perturbations. A KWANT system comprises a finite scattering region described by a scattering Hamiltonian H_S and infinite regions called leads (these represent the ohmic contacts in an experiment).

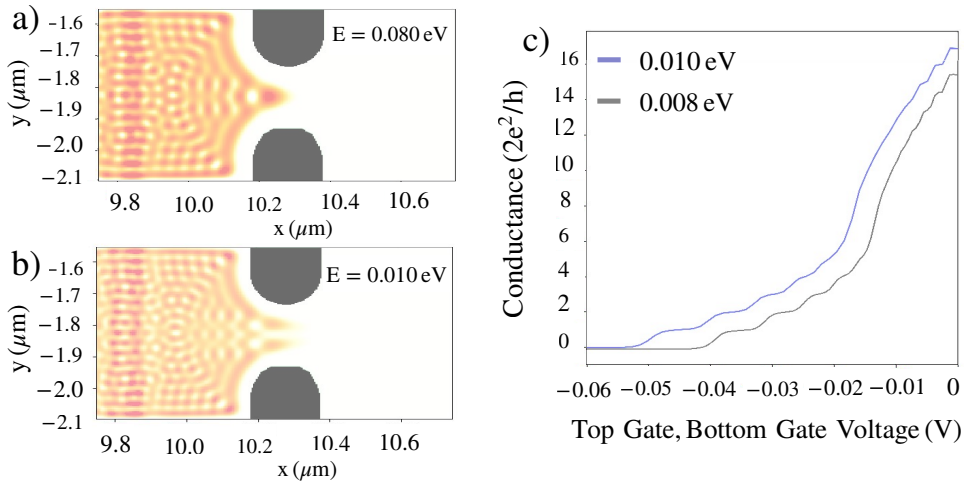


Figure B.4: (a) Calculated wavefunction squared at lower band energy such that a single channel propagates through the QPC. (b) Calculated wavefunction squared at increased band energy so that two channels propagate through the QPC. (c) Calculated conductance through the QPC at two energy bands as the voltage on both QPC gates is varied. Conductance drops to zero at lower gate potentials. Both curves show the characteristic QPC conductance plateaus at integer multiples of $2e^2/h$.

In the app, the KWANT system is generated by defining the lattice constant and lead locations. A plot of the system is shown in Fig. B.3a and corresponding band structure in Fig. B.3b. An energy level is selected to compute transport properties. A plot of the wavefunction squared is shown in Fig. B.4a, where a single channel is shown to propagate through the QPC. The calculated conductance at varying gate potentials is shown in Fig. B.4c,

B.3. Device Simulation

where the characteristic QPC conductance plateaus at integer multiples of $2e^2/h$ are found.